

# The Lighthill–Weis-Fogh clap–fling–sweep mechanism revisited

D. KOLOMENSKIY<sup>1</sup>†, H. K. MOFFATT<sup>2</sup>, M. FARGE<sup>3</sup>  
AND K. SCHNEIDER<sup>1,4</sup>

<sup>1</sup>M2P2–CNRS, Universités d’Aix-Marseille, 38 rue Joliot-Curie, 13451 Marseille CEDEX 20, France

<sup>2</sup>Department of Applied Mathematics and Theoretical Physics, University of Cambridge,  
Wilberforce Road, Cambridge CB3 0WA, UK

<sup>3</sup>LMD–IPSL–CNRS, Ecole Normale Supérieure, 24 rue Lhomond, 75231 Paris CEDEX 5, France

<sup>4</sup>CMI, Université de Provence, 39 rue Joliot-Curie, 13453 Marseille CEDEX 13, France

(Received 15 February 2010; revised 28 October 2010; accepted 11 February 2011)

The Lighthill–Weis-Fogh ‘clap–fling–sweep’ mechanism for lift generation in insect flight is re-examined. The novelty of this mechanism lies in the change of topology (the ‘break’) that occurs at a critical instant  $t_c$  when two wings separate at their ‘hinge’ point as ‘fling’ gives way to ‘sweep’, and the appearance of equal and opposite circulations around the wings at this critical instant. Our primary aim is to elucidate the behaviour near the hinge point as time  $t$  passes through  $t_c$ . First, Lighthill’s inviscid potential flow theory is reconsidered. It is argued that provided the linear and angular accelerations of the wings are continuous, the velocity field varies continuously through the break, although the pressure field jumps instantaneously at  $t = t_c$ . Then, effects of viscosity are considered. Near the hinge, the local Reynolds number is very small and local similarity solutions imply a logarithmic (integrable) singularity of the pressure jump across the hinge just before separation, in contrast to the ‘negligible pressure jump’ of inviscid theory invoked by Lighthill. We also present numerical simulations of the flow using a volume penalization technique to represent the motion of the wings. For Reynolds number equal to unity (based on wing chord), the results are in good agreement with the analytical solution. At a realistic Reynolds number of about 20, the flow near the hinge is influenced by leading-edge vortices, but local effects still persist. The lift coefficient is found to be much greater than that in the corresponding inviscid flow.

**Key words:** aerodynamics, low-Reynolds-number flows, swimming/flying

---

## 1. Introduction

Very small insects fly at much lower Reynolds number than larger insects, such as butterflies or dragonflies, and therefore have to develop different strategies for the maintenance of lift. One example is the chalcid wasp *Encarsia formosa*, used as a biological pesticide for the control of white fly (*Aleyrodidae*), a common pest of garden and greenhouse vegetables. The insect’s body is less than 1 mm long and its wings are about 1.5 mm in span (see Weis-Fogh 1973). It has two pairs of wings, the front and rear wings being hooked together and moving as one. As common

† Email address for correspondence: dkolom@gmail.com

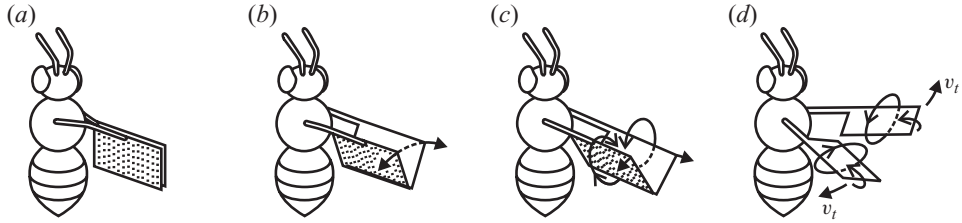


FIGURE 1. Schematic diagram showing clap (a), fling (b,c) and sweep (d) of *E. formosa*. Figures are adapted from Weis-Fogh (1973).

for small insects, each wing is enlarged along its edge by hairs, which entrain air, thus increasing the effective area without adding much extra weight. Through these hairs the insect actually senses the forces exerted by the flow (Chapman 1998) and probably uses this aerodynamic information to optimize its hovering motion. *E. formosa* flaps its wings at about  $400\text{ s}^{-1}$  by vibrating the muscles in its thorax. It has developed a morphology, for which the wings are mounted on flexible stalks and work as paddles, allowing for flapping motions that cannot be achieved by larger insects.

In one distinctive mode of motion, the insect adopts three successive movements during one downstroke, a ‘clap, fling and sweep’ of its wings, not unlike the human breaststroke used for swimming (see figure 1). Through this mechanism, the insect can potentially generate the lift and thrust that it needs to perform flight manoeuvres or to carry load. The wings first *clap* together behind the insect’s back, then open in a *fling* motion around the lower ‘hinge’, and finally separate at the hinge and *sweep* apart. At the end of this downstroke, the insect flips its wings up and translates them inwards until their leading edges join at the upper hinge. The main difference as compared with other hovering insects is that the flexible stalks on which its wings are mounted enable *E. formosa* to clap its wings together at the end of this upstroke.

Besides *E. formosa*, many other tiny insects perform this kind of motion too, e.g. the greenhouse whitefly *Trialeurodes vaporariorum* (Weis-Fogh 1975), thrips (Ellington 1984), the parasitoid wasp *Muscidifurax raptor* and the jewel wasp *Nasonia vitripennis* (Miller & Peskin 2009). Larger insects, such as locusts, may also use it (Cooter & Baker 1977).

This type of hovering motion was discovered by Weis-Fogh (1973) in his extensive study of insect flight, through the use of an ultra-fast camera (up to 8000 frames per second). Weis-Fogh observed that some hovering insects, and in particular *E. formosa*, generate larger aerodynamic forces – both lift and drag – than can be explained by traditional steady-state aerodynamics. He conjectured that a contact between the trailing edges may lead to favourable unsteady aerodynamic interactions. In collaboration with Lighthill, he described the essentials of this novel clap–fling–sweep hovering motion.

Lighthill (1973) argued that the clap–fling–sweep process provides a mechanism for the instantaneous generation of circulation and lift, even in the ‘ideal fluid’ situation in which the fluid is regarded as strictly inviscid and incompressible, and the flow irrotational ( $\text{curl } \mathbf{u} = 0$ ). This mechanism is associated with the separation of the wings at the lower hinge-point when fling begins to give way to sweep, as shown in figures 2 and 3. We shall refer to this instantaneous change of topology as ‘the break’, since it is at this moment that the wings break apart. Lighthill argued that, since the

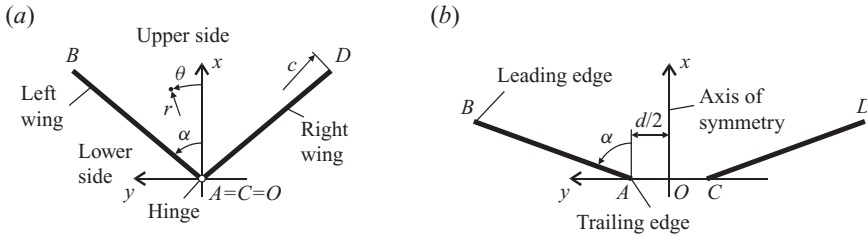


FIGURE 2. Sketch of a two-dimensional section of the wings during fling (a) and sweep (b). Note that  $\theta = 0$  on the axis  $y = 0$  ( $x > 0$ ) and that  $x = r \cos \theta$ ,  $y = r \sin \theta$ .

jump in pressure across the hinge is relatively small at the moment of separation, the circulation  $\pm \Gamma$  around each wing should be conserved, and close to that required ‘for generating maximum lift *at once* in the subsequent horizontal motion’ (our italics). The lift envisaged here is the Magnus lift  $\rho U \Gamma$  on each wing, where  $U$  is the ultimate steady outward wing speed during the sweep phase; of course it will take time, depending on the initial acceleration, for this speed to build up to its ultimate value.

As recognized by Lighthill and by subsequent authors (e.g. Maxworthy 1979), viscous effects associated with vortex shedding from the sharp edges of the wings during the complete periodic cycle of wing motion are also important in determining the time variation of the total circulation around each wing and the resulting lift force. However, the importance of the Lighthill–Weis-Fogh mechanism lies in the fact that it *can* operate in a *totally inviscid fluid* (however unrealistic such a medium may deem to be), that it provides a mechanism of lift generation associated with change of boundary topology (rather than with viscosity), and that it is therefore not subject to the Wagner effect, whereby the generation of lift is delayed until the process of viscous vortex shedding is accomplished (Wagner 1925). Thus, the key phenomenon is the apparently *instantaneous* generation of lift at the instant of wing separation.

In practice, viscous effects cannot be neglected, no matter how large the Reynolds number associated with the wing motion may be. As observed above, this is of course already well recognized in relation to the fundamental process of vortex shedding at sharp edges: the leading-edge separation during fling was first found experimentally by Maxworthy (1979), Spedding & Maxworthy (1986), and observed in numerical simulations by Haussling (1979). A modification of Lighthill’s theory was then proposed by Edwards & Cheng (1982) to account for the separated vortices.

We should mention that all hovering insect wings produce leading-edge vortices, but they become much stronger when the clap–fling–sweep is employed. This is because proximity of the trailing edges inhibits a counterflow past them. The flow phenomena at that location are very different from those usually observed near the trailing edges of conventional aerofoils, and deserve examination.

One can expect important viscous effects during the fling phase near the hinge point, which is a stagnation point on both sides of the hinge. For *E. formosa*, the hovering insect for which Weis-Fogh (1973) first identified the clap–fling–sweep process, the Reynolds number  $Re = \Omega c^2 / \nu$ , based on the wing angular velocity  $\Omega$ , the wing chord  $c$ , and the kinematic viscosity of the surrounding air  $\nu$ , is approximately 20. Near the hinge, the *local* Reynolds number is  $(r/c)^2 Re$ , and is therefore of order unity or smaller for  $r < 0.2c$ ,  $r$  being distance from the hinge. In this region viscous effects, far

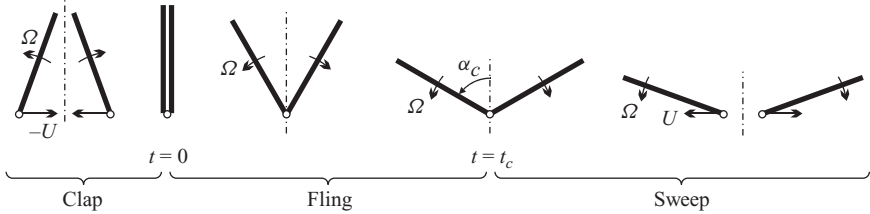


FIGURE 3. Two-dimensional idealization of the clap–fling–sweep motion of the wings.

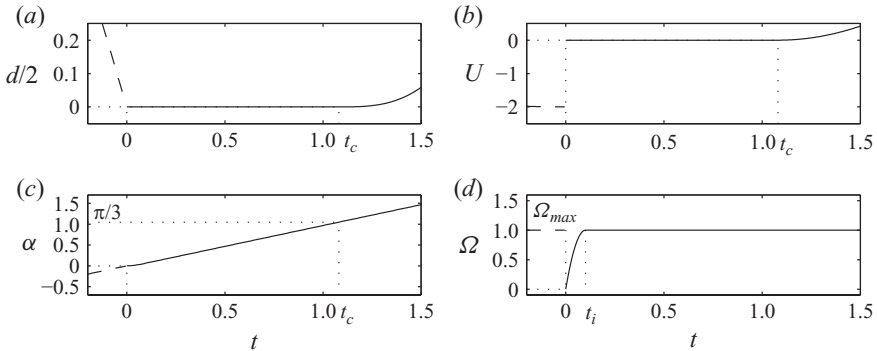


FIGURE 4. Kinematic parameters of the clap–fling–sweep motion: (a) half-distance between the trailing edges, (b) velocity of sweep, (c) angle of incidence and (d) angular velocity of the wings.

from being negligible, are in fact dominant, and may be expected to play a critical role in the local dynamics at the instant of separation. The Stokes flow near such a hinge point was first studied by Moffatt (1964), and further by Moffatt & Duffy (1980), where the distinction between contributions to the flow that are either locally or non-locally determined was recognized. The pressure field has a logarithmic singularity at the hinge-point (a singularity that can be resolved by taking account of non-sharpness of the corner), and the jump in pressure across the hinge before separation is infinite (positive or negative, depending on the angle), in profound contrast to the ‘negligible’ pressure difference identified by Lighthill for the ideal inviscid scenario, and again indicating a need to closely examine viscous effects near the hinge at the moment of separation. This is a prime aim of the present contribution.

First, however, it will be useful to consider some aspects of the two-dimensional, inviscid, irrotational flow scenario, as formulated by Lighthill. This is done in §2. Then, in §3, we proceed to the viscous case, and use Stokes approximation to derive local solutions for the flow. In §4, numerical simulations of the flow are presented and compared with the analytical results. Finally, conclusions are drawn in §5.

The computations presented in this paper are performed for an idealized motion of the wings designed to simplify the analysis of the flow shortly before and after the break. This motion is illustrated schematically in figure 3, and a time history of the kinematic parameters is shown in figure 4 (this refers to the left wing with unit chord length,  $c = 1$ ). Most of our discussion will concern only the stages of fling and sweep. Clap is only considered in §4.4 to provide an initial condition different from the state of rest. We adopt the convention that  $t = 0$  marks the beginning of the fling phase. During the clap (for  $t < 0$ ), the trailing edges move with horizontal

velocity  $U = -1 - \cos t$ , and the wings rotate with angular velocity  $\Omega = 1$ . At  $t = 0$ , the wings are vertical and fully clapped. Then fling begins, and the wings start rotating with an increasing angular velocity  $\Omega = 100(0.2t - t^2)$ . At time  $t_i = 0.1$ , the angular velocity reaches its maximum,  $\Omega_{max} = 1$ , and then remains constant. The angle of incidence mounts to  $\alpha = 60^\circ$  at  $t_c = (\pi + 0.1)/3 \approx 1.0805$ , and the wings break and sweep apart with an increasing velocity  $U = 2.4(t - t_c)^2$ , so that the distance  $d$  between the trailing edges increases like  $(t - t_c)^3$ . The angular velocity is kept constant through the initiation of sweep for the sake of simplicity. It is essential that  $\Omega$  and  $U$  are continuous through the break together with their derivatives, in order to guarantee no impulsive forces which the wings cannot sustain. Of course, the motion of real insect wings is much more complex. Numerical simulations of the flow past trailing edges of the wings with somewhat more realistic kinematics were reported recently by Kolomenskiy *et al.* (2010).

## 2. Inviscid fluid theory

We first review the potential flow theory for the fling phase, starting with a simple local analysis near the hinge point. Then we discuss the initiation of sweep.

### 2.1. Local analysis near the hinge

We use polar coordinates  $(r, \theta)$ , the wings  $AB$  and  $CD$  (see figure 2a) being at  $\theta = \alpha$  and  $\theta = -\alpha$ ,  $0 < r < c$ , and we shall suppose that  $\alpha < \pi/2$ ; the points  $A$  and  $C$  coincide during the fling phase. The wings fling open with angular velocities  $\pm\Omega$ , where  $\Omega = d\alpha/dt$ . Because of the symmetry about  $\theta = 0$ , we may focus attention throughout on the left-hand wing  $AB$ , and the flow in the region  $0 < \theta < \pi$ . The velocity field driven by the motion of the wings is assumed irrotational:

$$(u, v) = \nabla\phi = \left( \frac{\partial\phi}{\partial r}, \frac{1}{r} \frac{\partial\phi}{\partial\theta} \right), \quad \text{with} \quad \nabla^2\phi = 0. \quad (2.1)$$

Near the hinge  $A$ , we may suppose that the flow should be determined solely by  $\alpha$  and  $\Omega$ , and on dimensional grounds, then the potential must take the form

$$\phi_1 = A_1 \Omega r^2 f(\theta), \quad (2.2)$$

where  $A_1$  is a dimensionless constant dependent only on  $\alpha$ . Symmetry about  $\theta = 0$  and the boundary condition

$$\frac{1}{r} \frac{\partial\phi_1}{\partial\theta} = \Omega r \quad \text{on} \quad \theta = \alpha, \quad (2.3)$$

then determine  $\phi_1$  in the form

$$\phi_1 = -\frac{\Omega}{2 \sin 2\alpha} r^2 \cos 2\theta. \quad (2.4)$$

This is a (local) similarity solution of the *first kind*, in the terminology of Barenblatt (1979), and it is a uniform straining flow with hyperbolic streamlines whose asymptotes are parallel and perpendicular to the bisector of the hinge angle. This *is* in fact the correct asymptotic form for the flow on the upper side of the wings  $|\theta| < \alpha$ , but *not* on the lower side  $|\theta| > \alpha$ , as will now be explained.

We may add to  $\phi_1$  any solution  $\phi_2$  of the homogeneous problem

$$\nabla^2\phi_2 = 0, \quad \frac{1}{r} \frac{\partial\phi_2}{\partial\theta} = 0, \quad \text{on} \quad \theta = \alpha, \quad (2.5)$$

and on the upper side of the wings, one such solution with the appropriate symmetry is

$$\phi_2 = A_2 r^q \cos q\theta, \quad \text{with } q = \pi/\alpha. \quad (2.6)$$

Here  $A_2$  is a constant with dimensions  $(\text{length})^{2-q}$ , which cannot be determined by local considerations alone. It is influenced by conditions remote from the hinge, and is, again in Barenblatt's terminology, a similarity solution of *the second kind*. However, since  $q > 2$ , the velocity field  $\mathbf{u}_2 = \nabla\phi_2$  is negligible compared with the field  $\mathbf{u}_1 = \nabla\phi_1$  sufficiently near the corner and (2.4) does therefore provide the dominant contribution to the flow in this region.

The situation is different on the lower side  $|\theta| > \alpha$ . Here, the solution analogous to (2.6) and with the appropriate symmetry is

$$\phi'_2 = A'_2 r^q \cos q(\pi - \theta), \quad \text{where now } q = \pi/(\pi - \alpha) < 2. \quad (2.7)$$

This term dominates over  $\phi_1$  sufficiently near the hinge and provides the dominant contribution to the flow on the lower side. The only problem is that the coefficient  $A'_2$  is influenced by remote conditions and cannot be determined by local analysis alone.

The difference between  $\phi_1$  and  $\phi'_2$ , and the corresponding jump in tangential velocity  $\partial\phi/\partial r$  across either wing, provides a contribution to the 'bound vorticity', equal and opposite in sign, within the two wings. The distribution of bound vorticity over the whole wings may be expected to provide a flow which, at a large distance from the wings, should have dipole form; this is confirmed below.

## 2.2. Some aspects of Lighthill's fling solution

Guided by the above discussion, let us now consider some properties of Lighthill's solution for the irrotational flow during the fling phase (for notation, see figure 3 and also Lighthill 1973). We note a misprint in Lighthill's equation (2) defining the Schwarz–Christoffel transformation between the upper half of his cut  $z$ -plane and the upper half of the  $Z$ -plane, which should correctly read as

$$\frac{dz}{dZ} = K \left( \frac{Z-1}{Z+1} \right)^{\alpha/\pi} \frac{Z-a}{Z-1}, \quad (2.8)$$

with  $a = 1 - 2\alpha/\pi$ . As pointed out by Edwards & Cheng (1982), this transformation, which has singularities at  $Z = -1$ ,  $a$  and  $1$ , can be integrated explicitly to give

$$z = K(1+Z)^{1-\lambda}(Z-1)^\lambda, \quad \text{where } \lambda = \alpha/\pi < 1/2. \quad (2.9)$$

The validity of (2.9) may be easily verified by direct differentiation (note that there are errors and/or misprints in (1) of Edwards & Cheng (1982), but (4) is correct therein). The constant  $K$  is fixed by the requirement that the point  $Z = a$  maps to the point  $z = c e^{i\alpha}$ , i.e.

$$K = \frac{c}{2}(1-\lambda)^{\lambda-1}\lambda^{-\lambda}, \quad (2.10)$$

where  $c$  is the chord of the wing. Note that  $Z (= X + iY)$  is a dimensionless complex variable, whereas  $z (= x + iy = r e^{i\theta})$  has the same dimension as  $K$  and  $c$ , i.e. length.

The instantaneous complex potential  $w = \phi + i\psi$  corresponding to angular velocity  $\Omega = d\alpha/dt$  is then given by

$$w(z) = \frac{\Omega K^2}{2\pi} \int_{-1}^1 (1+t)^{2-2\lambda}(1-t)^{2\lambda}(Z-t)^{-1} dt, \quad (2.11)$$

where  $Z$  is given in terms of  $z$  by the inverse mapping associated with (2.9). Edwards & Cheng (1982) gave an explicit expression for this integral in the form

$$w = \frac{\Omega K^2}{2 \sin 2\alpha} (-(Z+1)^{2-2\lambda}(Z-1)^{2\lambda} + Z^2 + 2Z(1-2\lambda) + \text{const.}), \quad (2.12)$$

where the integration constant equals  $2\alpha^2 - 1$  if we require  $w$  to vanish at infinity. From (2.12), it is straightforward to obtain formulae for the complex velocity,  $u - iv = dw/dz$ , and for the pressure,

$$p = -\rho \left( \frac{\partial \phi}{\partial t} + \frac{|u - iv|^2}{2} \right), \quad (2.13)$$

where  $\rho$  stands for the density of the fluid, and the ambient pressure is zero.

Alternatively, the complex potential  $w$  can be expressed in terms of the Gauss hypergeometric function  $F$  (Gradshteyn & Ryzhik 1980, p. 290, 3.228, equation 3):

$$w = -\frac{8\Omega K^2 \lambda(1-\lambda)(1-2\lambda)}{3 \sin 2\alpha(1-Z)} F\left(1, 2\lambda+1; 4; \frac{2}{1-Z}\right). \quad (2.14)$$

This function is analytic in the complex  $Z$ -plane cut along the real axis from  $-1$  to  $1$ . Note that for  $|Z| \gg 1$ ,  $z = KZ + O(1)$  and (2.14) gives

$$w = \frac{8\Omega K^3 \lambda(1-\lambda)(1-2\lambda)}{3 \sin 2\alpha} \frac{1}{z} + O(z^{-2}), \quad (2.15)$$

in which the leading term is the complex potential of a dipole directed towards the origin along the line  $\theta = 0$ , as anticipated from the discussion of §2.1. This can be thought of either as a vortex dipole associated with the equal and opposite bound vorticity distributions in the two wings, or as a source–sink dipole, the source being on the lower side of the wings and the sink on the upper side while the angle  $\alpha$  is increasing. Lighthill recognized the sink character of the flow into the opening angle when it is small, but his sketch of the flow structure in his figure 5 is seriously misleading. In fact, each streamline of the flow in the half-plane  $0 < \theta < \pi$  starts from a point  $z = r e^{i\alpha}$  ( $0 < r < c$ ) on the lower side of the wing  $\theta = \alpha$  and, by virtue of incompressibility, ends at the same point  $r e^{i\alpha}$  on the upper side. This can be seen in figure 5, which displays the streamlines and the iso-potential lines corresponding to (2.12). One can also observe the dipolar character of the flow far-field.

We may use (2.12) to determine the asymptotic nature of the flow near the hinge point  $A$ . Thus, near  $Z = -1$ , it gives

$$w \approx -\frac{\Omega K^2}{2 \sin 2\alpha} ((-2)^{2\lambda}(Z+1)^{2-2\lambda} + 4\lambda(Z+1) + (Z+1)^2 + \text{const.}'), \quad (2.16)$$

and (2.9) gives

$$z \approx K(-2)^\lambda(Z+1)^{1-\lambda}. \quad (2.17)$$

Hence, approaching the hinge point  $z = 0$  from the lower side, we have

$$w(z) \approx -\frac{\Omega K^2}{2 \sin 2\alpha} \left\{ 4\lambda \left( \frac{z}{K(-2)^\lambda} \right)^q + \left( \frac{z}{K} \right)^2 + \dots \right\}, \quad \text{with } q = \frac{1}{1-\lambda}, \quad (2.18)$$

which simplifies to

$$w(z) \approx 2^{\alpha q} \frac{\Omega K^2 \lambda}{\sin 2\alpha} \left( \frac{-(ze^{-i\alpha})^q}{K^q} \right) - \frac{\Omega}{2 \sin 2\alpha} z^2 + \dots. \quad (2.19)$$

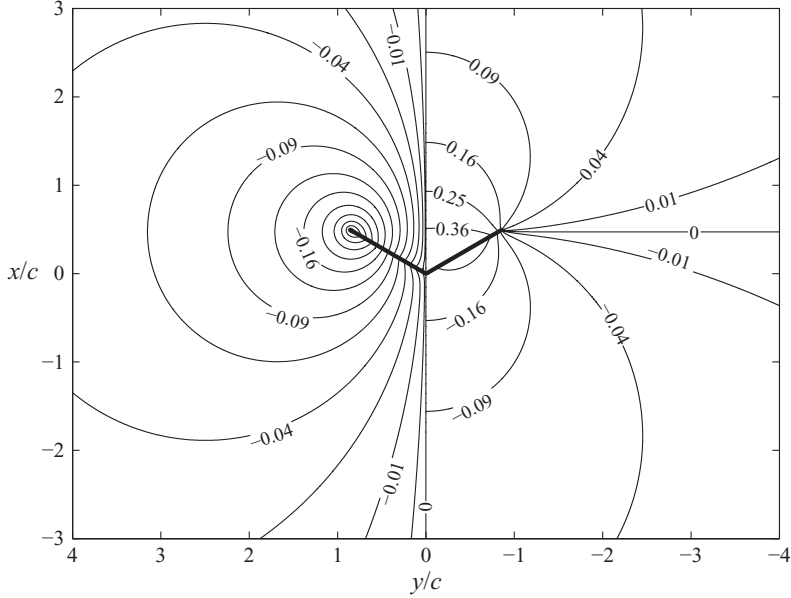


FIGURE 5. Streamlines (left half of the figure) and iso-potential lines (right half) of Lighthill's solution. The values are normalized by  $\Omega c^2$ . The axis of symmetry is the  $x$ -axis, for consistency with (2.9).

This is in total agreement with the asymptotics described in §2.1, the coefficient  $A'_2$  being now determined as

$$A'_2 = 2^{aq} \frac{\Omega K^{2-q}}{\sin 2\alpha} \lambda. \quad (2.20)$$

The fact that  $A'_2 > 0$  implies that the dominant streaming flow described by the potential (2.7) is *towards* the hinge point at  $\theta = \alpha$ . Note, again, that the first term in (2.19) dominates because  $q < 2$ .

Similar asymptotics may be carried out near  $Z = +1$ , i.e. near  $z = 0$  on the upper side. Again, the results are in total agreement with those of §2.1, the dominant term in this region being the uniform strain term proportional to  $z^2$ .

There is however a puzzle here: the jump in the radial component of velocity across the left-hand wing  $AB$  near  $r = 0$  from the lower to the upper side is positive and so gives a positive (anticlockwise) contribution to the bound vorticity in that wing. However, the *total* bound vorticity in this wing must be negative (clockwise) to account for the direction of the dipole flow at a large distance. Hence, there must be a greater negative contribution to the bound vorticity near the end of the wing at  $z = c e^{i\alpha}$ .

To confirm this, we need to consider the asymptotics near  $Z = a = 1 - 2\lambda$ . Setting  $Z = a + \zeta$  where  $|\zeta| \ll 1$ , we first find, from (2.9), that

$$z = c e^{i\alpha} \left[ 1 - \frac{\zeta^2}{8\lambda(1-\lambda)} + \dots \right] \quad (2.21)$$

and then, from (2.12), that

$$w \approx \frac{4\Omega K^2}{\sin 2\alpha} \left\{ \pm(1-2\lambda)\sqrt{2\lambda(1-\lambda)} \left(1 - \frac{z}{c e^{i\alpha}}\right)^{1/2} + \text{const.}'' + \dots \right\}. \quad (2.22)$$



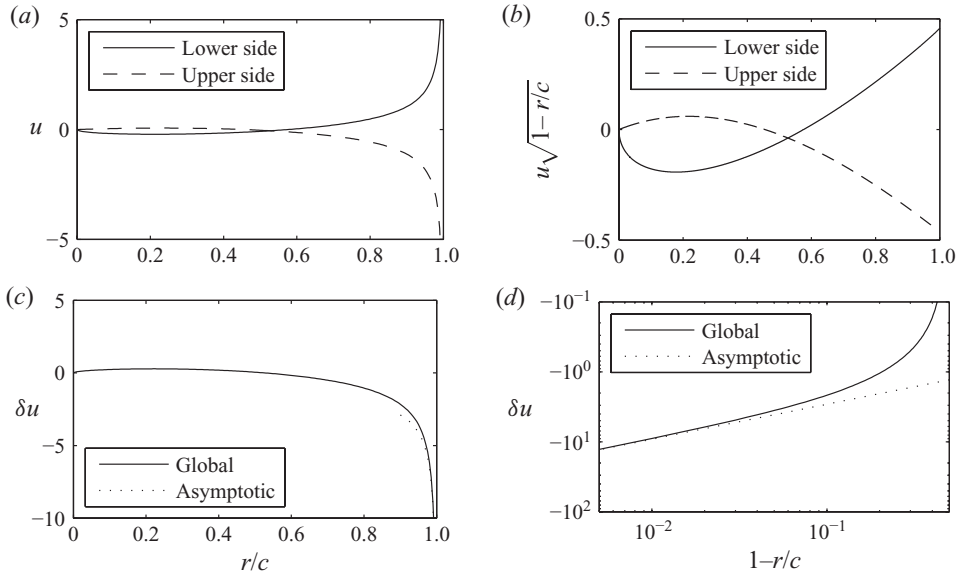


FIGURE 6. (a) Radial velocity  $u(r/c)$ , (b)  $u\sqrt{1-r/c}$ , (c) radial velocity jump  $\delta u = u_u - u_l$  and its asymptote (2.23) and (d) magnitude of the radial velocity jump  $\delta u$  shown in logarithmic scale near  $r/c = 1$ .

The jump in the radial velocity from the lower to the upper side of the wing at position  $z = re^{i\alpha}$  is then easily obtained in the form

$$\delta u = u_u - u_l \approx -\frac{4\Omega K^2}{\sin 2\alpha} \frac{1-2\lambda}{c} \sqrt{2\lambda(1-\lambda)} \left(1 - \frac{r}{c}\right)^{-1/2}, \quad (2.23)$$

where  $u_u$  and  $u_l$  are the radial velocities on the upper and the lower sides, respectively. This is singular at  $r = c$  (as for any ideal flow around a salient edge), but the singularity is integrable, and the integrated contribution to the bound vorticity from this region is indeed negative as expected.

This is confirmed by figure 6, drawn for  $\lambda = 1/3$ . The solid line in figure 6(a) shows the radial velocity  $u_l$  (normalized by  $\Omega c$ ) on the lower side of the wing as a function of  $r/c$ , slightly negative over approximately 50% of the chord near the hinge, but with a region of strong positive velocity (singular at  $r/c = 1$ ) over 50% near the leading edge; the dashed line shows the radial velocity  $u_u$  on the upper side of the wing, which has the same singularity near  $r/c = 1$ , but of opposite sign. The strength of the bound vortex sheet (i.e. the jump in the radial velocity across the wing) is concentrated in this outer 50% of the wing, and is negative there (for the left-hand wing), giving the required sign for the remote dipole field.

Figure 6(b) shows  $u\sqrt{1-r/c}$  on both sides of the wing, confirming that the singularity is indeed of the expected kind at  $r/c = 1$ . This also shows that the negative contribution on the lower side is much greater (in magnitude) than that on the upper side near  $r/c = 0$ , as expected from the local analysis near the hinge point. The radial velocity jump is shown in figure 6(c) and its singular behaviour is magnified in figure 6(d), displayed in a logarithmic scale to reveal the  $(c-r)^{-1/2}$  asymptotics.

The far-field asymptotic expansion (2.15) is useful to calculate the lift force acting on the wing. The total fluid-dynamic force, as given by Sedov (1965), in the case of

thin wings equals

$$F = \frac{i\rho}{2} \oint_C \overline{\left(\frac{dw}{dz}\right)^2} dz + i\rho \frac{d}{dt} \oint_C z \frac{dw}{dz} dz. \quad (2.24)$$

The integrals are taken over any curve  $C$  enclosing the wing; the overbar signifies the complex conjugate. Supposing that  $C$  consists of the real axis and a half-circle of indefinitely large radius, and noting that only the half-circle contributes to the lift  $L = \text{Re } F$ , the following formula can be obtained:

$$L = \frac{\pi\rho c^3(1-\lambda)^{3\lambda-2}}{3\lambda^{3\lambda-1} \sin 2\alpha} \left\{ \Omega^2 a + \frac{\Omega^2}{\pi} \left[ \frac{1}{\lambda(1-\lambda)} + 3a \ln \frac{1-\lambda}{\lambda} - \frac{2\pi a}{\tan 2\alpha} - 6 \right] \right\}, \quad (2.25)$$

which is equivalent to the formula for the lift first derived by Wu & Hu-Chen (1984). Note that, when  $\Omega$  is constant in time,  $L$  decreases monotonically and vanishes at  $\alpha = \pi/2$ .

### 2.3. Initiation of sweep

We are now in a position to describe exactly what happens at the critical moment of separation of the wings, still within the framework of ideal fluid theory. This is the moment  $t_c$  of initiation of the ‘sweep’ phase, for which we may suppose that the separation  $d(t)$  of the lower (‘trailing’) edges of the wings initially increases smoothly in proportion to  $(t - t_c)^3$  (corresponding to linearly increasing outward acceleration of the wings). Suppose the break occurs when  $\alpha = \alpha_c$  and  $\Omega = \Omega_c$ , and that both  $\alpha$  and  $\Omega$  are continuous and smooth through the break.

Just before the break, the circulation  $\Gamma$  around the wing  $AB$  from the stagnation point on the upper side of the hinge to that on the lower side is

$$\Gamma = -\Omega c^2 g(\lambda), \quad \text{with } \lambda = \alpha/\pi, \quad (2.26)$$

where the function  $g(\lambda)$  is as computed by Lighthill. As shown by Edwards & Cheng (1982), this function has the explicit form

$$g(\lambda) = \frac{1 - 2\lambda}{2(\sin 2\pi\lambda)\lambda^{2\lambda}(1-\lambda)^{2-2\lambda}}. \quad (2.27)$$

Note that  $g(1/2) = 2/\pi \approx 0.636$ , and that near  $\lambda = 1/2$ ,

$$g(\lambda) \approx \frac{2}{\pi} + \frac{1}{2} \left( \lambda - \frac{1}{2} \right)^2 g_c'', \quad \text{where } g_c'' = \frac{8(\pi^2 - 6)}{3\pi} \approx 3.285. \quad (2.28)$$

This is a good approximation even at  $\lambda = 1/3$  (or  $\alpha = \pi/3$ , the angle near which the wings of *E. formosa* are observed to separate).

Lighthill further showed that the jump increase in pressure  $\delta p$  across the hinge from the lower to the upper side is given (before the break) by

$$\delta p = \rho \frac{d\Gamma}{dt} = -\frac{\rho\Omega^2 c^2}{\pi} g'(\lambda), \quad (2.29)$$

and he commented that this is small in the range of  $\lambda$  of entomological interest; for example, when  $\lambda = 1/3$ , this gives  $\delta p/\rho\Omega^2 c^2 \approx 0.174$ . Whether this is small or not is perhaps a matter of taste.

When the break occurs, this pressure jump is no longer sustainable; within the framework of the incompressibility assumption, it is instantaneously spread over the fluid in such a way that the condition

$$\nabla^2 [p + (1/2)\rho|\nabla\phi|^2] = 0 \quad (2.30)$$

is satisfied, as follows from the Bernoulli integral for the potential flow. The velocity is continuous through the moment of separation, but the fluid acceleration is discontinuous due to the temporal jump in  $\nabla p$  resulting from this instantaneous redistribution of pressure. In particular, fluid accelerates from a state of near rest in the neighbourhood of the opening gap, the flux  $Q(t)$  through the gap increasing from zero at  $t = t_c$ . If the gap  $d(t)$  increases initially like  $(t - t_c)^3$ , and the mean fluid velocity through the gap increases like  $(t - t_c)^2$ , then  $Q$  increases initially like  $(t - t_c)^5$ .

The circulation  $\pm\Gamma$  around the surface of each wing is continuous through  $t = t_c$ , since no impulse is applied to the fluid. Restricting attention to the left-hand region immediately after the break, this circulation remains equal to  $\Gamma$  in the subsequent sweeping motion since the flow remains irrotational; this is the basis of the Lighthill–Weis-Fogh mechanism. Note however that, contrary to the impression conveyed by Lighthill, there would appear to be no need (for the validity of the argument) for the pressure jump  $\delta p$  to be negligibly small across the hinge before the break; we require only the break to be smooth and impart no impulsive force to the fluid.

Although the velocity field is continuous through the break, its potential  $\phi$  undergoes a curious transition: before the break,  $\phi$  is single-valued, whereas after the break it is multiple-valued because of the circulations around the now separated wings. We can, of course, artificially replace  $\phi$  just before the break by the set of functions  $\{\phi + n\Gamma\}$ , where  $n$  is any integer positive, zero, or negative, for each of which  $\mathbf{u} = \nabla\phi$  is the same field; then the transition to the multiple-valued  $\phi$  just after the break becomes more easily comprehensible, the *set* of functions then changing in a continuous manner (everywhere, except at the hinge point).

During the outward sweep, flip and inward sweep that follows the break, the circulation around every closed circuit in the fluid that embraces the left-hand wing once (and does not embrace the right-hand wing) remains constant and equal to  $\Gamma$ . It should be recognized however that, for so long as the wing is in motion outwards, streamlines starting on the lower side of the wing must end at the corresponding point on the upper side, just as they did before the break (a consequence of incompressibility, as noted previously). There are now however some streamlines that pass through the gap (those contributing to the flux  $Q(t)$ ), and on these streamlines, some of which extend to the far (dipolar) field, the circulation is  $\Gamma$ .

If the wings were to be brought to rest in the separated position, then no streamlines would start or end on the wings, and every streamline would be a closed curve enclosing a wing. In this situation, the flux  $Q$  would be steady and proportional to  $\Gamma$ , and otherwise determined by the position of the wings. Each wing in such a situation would find itself in the downflow of the circulation about the other wing, and would experience a horizontal force of attraction to the other wing. There can be no vertical lift force in this steady situation because the momentum in the fluid is constant and the flux of momentum ‘to infinity’ associated with the remote dipole field is zero.

Of course, in practice the wings do not come to rest: they sweep outwards, then flip, then sweep inwards, making renewed contact at the upper (‘leading’) edges. On ideal theory, the circulation remains constant throughout this movement and persists as circulation around the wings even until the moment of the renewed contact.

#### 2.4. Sweep

Just like during the fling, the flow during the sweep phase can be analysed using conformal mapping techniques, as recently proposed by Crowdy (2009). We follow this approach with slight modifications, described in Appendix A. We also used a vortex method to verify some results.

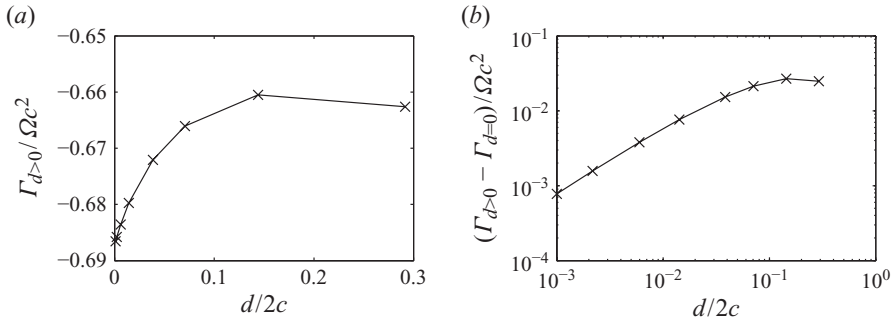


FIGURE 7. (a) Circulation  $\Gamma_{d>0}$  around the wing (normalized by  $\Omega c^2$ ); (b) its difference with respect to  $\Gamma_{d=0}$  obtained from Lighthill's model.

In view of the above discussion, it is instructive to match the solution during sweep at  $t \downarrow t_c$  with Lighthill's solution at  $t \uparrow t_c$ . An important question is whether the circulation  $\Gamma$  after the break is equal to the value given by (2.26) before the break. To clarify this, let us first consider a hypothetical situation in which there is a non-zero distance  $d$  between the trailing edges, but there is no translational motion, i.e.  $U = 0$ . The two wings rotate about their trailing edges with angular velocities  $+\Omega$  and  $-\Omega$ , and their angles of incidence equal  $+\alpha$  and  $-\alpha$ , respectively. Let us fix the value of  $\Gamma$  by requiring the velocity to vanish at the trailing edges (thus we remove singularities from them). In these circumstances, one can expect that, in the limit of  $d \rightarrow 0$ , the flow given by (A 10) converges to (2.12).

Figure 7(a) displays the required values of the circulation  $\Gamma_{d>0}$  (normalized by  $\Omega c^2$ ) as a function of distance  $d$  at  $\alpha = \pi/3$ . Apparently, it is converging to the value  $\Gamma_{d=0} \approx -0.687 \Omega c^2$  given by (2.26)–(2.27). Figure 7(b) presents the difference in logarithmic scale. It suggests a power law  $\Gamma_{d>0} - \Gamma_{d=0} \propto d^m$ ,  $m < 1$ ; the exact value of  $m$  presumably depends on  $\lambda$ .

Returning to the flow due to two wings which break apart at time  $t_c$ , it is essential that the circulation  $\Gamma$  around a wing must remain constant when  $t > t_c$ . Lighthill argued that this constant is  $\Gamma_{d=0}$ . Actually, there are singularities at the trailing edges when  $d > 0$ , but as  $d$  tends to zero, the velocity everywhere within the fluid also converges to its value at  $d = 0$ . It follows that the flow that evolves continuously through the break is indeed the one that occurs when the wings carry the circulations they had just before the break.

Once the circulation is fixed to  $\Gamma = \Gamma_{d=0}$ , we can proceed with our analysis of the flow during sweep. In what follows, we fix  $c = 1$ ; the results can easily be scaled to any chord length. The motion of the wings is described in § 1 (see figure 4 and the discussion related to it).

Figure 8 shows streamlines at  $t = 1.5$ , when the half-distance between the trailing edges  $d/2 \approx 0.059$ . The dipolar far-field is dominated by bound vortices at the leading edges, as during fling (cf. figure 5). The circulation around a wing is prescribed at its value at  $t = t_c$ , which fails to ensure zero velocity at the trailing edges. A zoom at  $z = 0$  indeed reveals a vortex at  $z_{te}$ . Its contribution to the overall circulation  $\Gamma$  is small, but the velocity at the trailing edge becomes infinite, no matter how small  $d$  is (although zero in the limit  $d \rightarrow 0$ ). This singularity can be removed by a particular choice of  $U(t)$ , as suggested by Crowdy (2009). However, such a velocity necessarily diverges at  $t = t_c$ , and therefore fails to fulfil our requirements on the smoothness of the transition from fling to sweep.

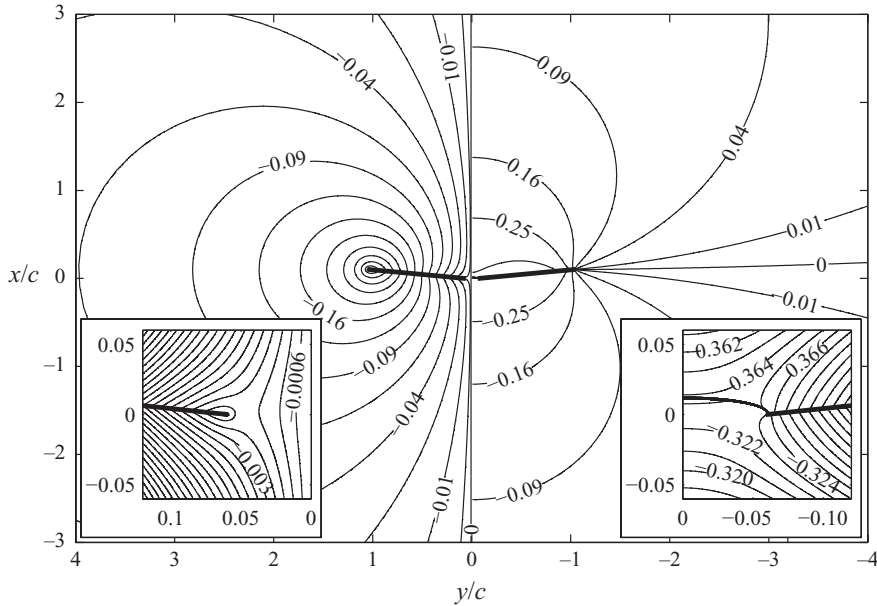


FIGURE 8. Streamlines (left half of the figure) and iso-potential lines (right half) during sweep at  $t = 1.5$ . The values are normalized by  $\Omega c^2$ . Note that the potential is multi-valued with a cyclic constant  $\Gamma \approx -0.687 \Omega c^2$ . The left inset shows streamlines near the trailing edge, starting from the zeroth line which coincides with the axis of symmetry, and drawn with a constant step  $\delta\psi = -0.0006$ . The right inset displays iso-potential lines drawn with a constant step  $\delta\phi = 0.001$ .

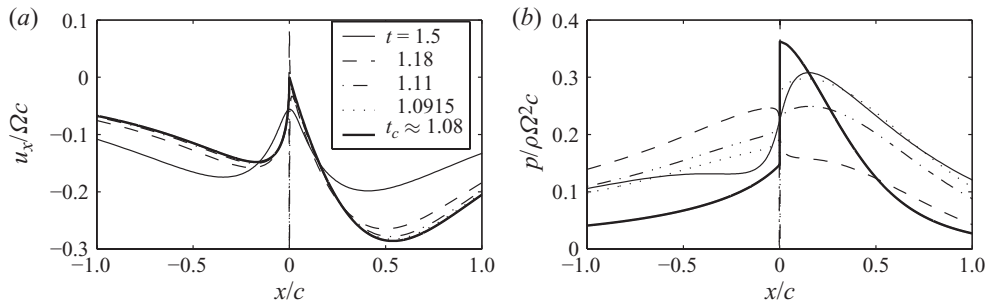


FIGURE 9. Velocity (a) and pressure (b) along the axis of symmetry.

Further insight into the flow near the trailing edges is provided by the  $x$ -velocity and pressure profiles along the axis of symmetry ( $\text{Im } z = 0$ ), displayed in figure 9. Figure 9(a) makes evident the continuous change of the velocity everywhere in the fluid: the curves corresponding to  $t > t_c$  converge to the values of  $Re dw/dz$  obtained from (2.12), with  $\alpha$  and  $\Omega$  as in figure 4 at  $t = t_c \approx 1.08$ . Overshoots near  $z = 0$  indicate the expected singularity at the trailing edge.

Meanwhile, the pressure changes in time more rapidly. This is shown in figure 9(b). Even at  $t = 1.0915$ , when  $d/2 \approx 1.06 \times 10^{-6}$ , the departure from the pressure distribution at  $t = t_c$  is significant. Before the break there is a discontinuity at  $z = 0$ ; it disappears immediately after the break, but the gradient remains sharp until the wings are sufficiently far from each other.

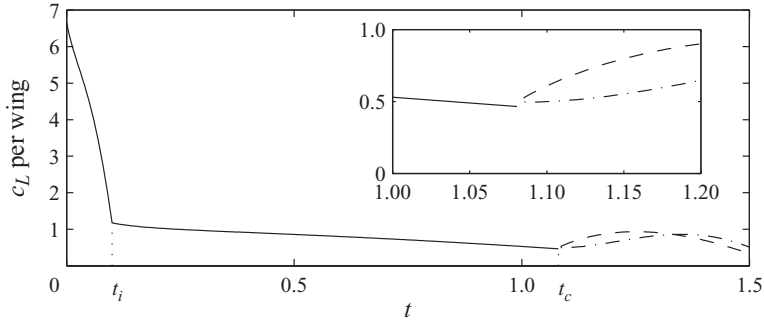


FIGURE 10. Lift coefficient per wing, generated during fling (solid line), during sweep with  $U = 2.4(t - t_c)^2$  (dash) and with  $U = 5.7(t - t_c)^3$  (dash-dotted) in an inviscid fluid.

The pressure during sweep is likely not to converge to its values during fling, for the following reason. The steady term  $-\rho|dw/dz|^2/2$  in (2.13) changes continuously through the break, because the velocity does so. However, the unsteady term  $-\rho\partial\phi/\partial t$  depends on  $\dot{\Gamma} = d\Gamma/dt$ , which is discontinuous. Note that if the sweep started at  $\alpha = \pi/2$ , the circulation  $\Gamma$  would evolve continuously in time, and so would the pressure.

The lift coefficient per wing,  $c_L = 2L/\rho\Omega_{max}^2 c^3$ , is shown in figure 10. The solid line corresponds to fling. It starts from  $c_L = 20/3$ , and during  $t \ll t_c$  the first term in the expression within curly brackets in (2.25) is dominant. This component decays as both  $a$  and  $\Omega$  decrease, and vanishes at  $t = t_i$ . Then,  $c_L$  continues to slowly decrease as a consequence of the decreasing circulation around a half-wing, until the wings break apart at  $t_c$ .

The lift coefficient during sweep is only calculated for  $t > 1.085$ . Two motion laws are compared:  $U = 2.4(t - t_c)^2$  and  $U = 5.7(t - t_c)^3$ . The lift coefficient begins to increase after the break, because now the circulation remains constant and, moreover, the wings start to move with an increasing velocity  $U$  (while continuing to rotate with angular velocity  $\Omega$ ). For  $U = 2.4(t - t_c)^2$ ,  $c_L$  decreases again after  $t \approx 1.25$ , when the angle  $\pi/2 - \alpha$  becomes small. For  $U = 5.7(t - t_c)^3$ , the initial growth is slower and the peak is delayed. A zoom at  $t_c$  reveals a small discontinuity of  $c_L$ , presumably a consequence of the jump in pressure at  $t = t_c$ .

The time history of the lift coefficient not only confirms Lighthill's conclusion that the clap–fling–sweep mechanism can operate in an inviscid fluid, but also gives a quantitative measure of its validity, which can be directly compared to similar results for a viscous fluid. This has been done in §4. More examples of the inviscid mechanism are discussed in Appendix B.

To conclude this section, we should mention a possibility to modify (A 10) using a point-vortex model of the leading-edge viscous separation (see e.g. Edwards & Cheng 1982; Michelin & Llewellyn Smith 2009). However, near the trailing edges, viscous effects are of a different kind.

### 3. Analysis of viscous effects near the break point

In a similar vein, let us now return to the break point, and enquire how the process described above is modified by viscous effects. As indicated in the Introduction, viscous vortex shedding from the sharp leading edges of the wings is important; in this process, the vorticity that is shed is essentially that which would otherwise be

contained in boundary layers on the upper side of the wings near the leading edges. In contrast, the boundary layers near the leading edges on the lower side remain attached, being in a region of decreasing pressure and rapid acceleration. A small amount of (equal and opposite) vorticity may be swept downwards and outwards from the lower side of the wings in the hinge region after the wings sweep apart (see Kolomenskiy *et al.* 2010).

### 3.1. Local similarity solution for fling

We now focus on the hinge neighbourhood on both sides of the wings. As pointed out in the Introduction, the local Reynolds number is small ( $O(\Omega r^2)$ ) in this region, and the Stokes approximation is appropriate. We use a streamfunction  $\psi(r, \theta)$ , with velocity components

$$u = r^{-1} \partial \psi / \partial \theta, \quad v = -\partial \psi / \partial r. \quad (3.1)$$

In the Stokes approximation, this satisfies the biharmonic equation

$$\nabla^4 \psi = 0, \quad (3.2)$$

on both sides from the hinge, and the boundary conditions

$$u = 0, \quad v = \Omega r, \quad \text{on } \theta = \alpha (\leq \pi/2), \quad (3.3)$$

and also the symmetry condition

$$\psi(r, \theta) = -\psi(r, -\theta). \quad (3.4)$$

The solution to this problem was given by Moffatt (1964); on the upper side of the wings, it takes the form (a similarity solution of the first kind)

$$\psi = \frac{1}{2} \Omega r^2 f(\theta) \quad \text{with} \quad f(\theta) = -\frac{\sin 2\theta - 2\theta \cos 2\alpha}{\sin 2\alpha - 2\alpha \cos 2\alpha}. \quad (3.5)$$

The associated vorticity  $\omega = -\nabla^2 \psi$  takes the remarkably simple form

$$\omega = \frac{-4\Omega\theta}{\tan 2\alpha - 2\alpha}, \quad (3.6)$$

and the pressure field is then given by

$$\frac{\partial p}{\partial r} = \frac{\mu}{r} \frac{\partial}{\partial \theta} \nabla^2 \psi = \frac{4\mu\Omega}{\tan 2\alpha - 2\alpha} \left( \frac{1}{r} \right), \quad \text{i.e.} \quad p = \frac{-4\mu\Omega}{\tan 2\alpha - 2\alpha} \ln \frac{C}{r}, \quad (3.7)$$

where  $C$  is an integration constant. This is of course simply an asymptotic behaviour near  $r = 0$ . Note that the coefficient of the logarithmic term in (3.7) vanishes and then changes sign as  $\alpha$  increases through  $\pi/4$ .

Similarly, on the lower side, we simply replace  $\theta$  by  $\pi - \theta$  and  $\alpha$  by  $\pi - \alpha$  in the above solution, giving a local pressure field

$$p = \frac{-4\mu\Omega}{2(\pi - \alpha) + \tan 2\alpha} \ln \frac{C}{r}. \quad (3.8)$$

Here, the singularity at the value of  $\alpha$  for which  $2(\pi - \alpha) = -\tan 2\alpha$ , namely  $\alpha \approx 51.3^\circ$  ( $\pi - \alpha \approx 128.7^\circ$ ), must be noted; for  $\pi - \alpha > 128.7^\circ$ , as explained by Moffatt & Duffy (1980), the solution (3.5) gives way, with a logarithmic transition through the critical angle, to a similarity solution of the second kind, which then dominates near the corner on the lower side. However, in the range of angles at which the break occurs for hovering insects ( $\pi - \alpha \approx 120^\circ$ ), the behaviour (3.8) is applicable and this is the expression that we shall use.

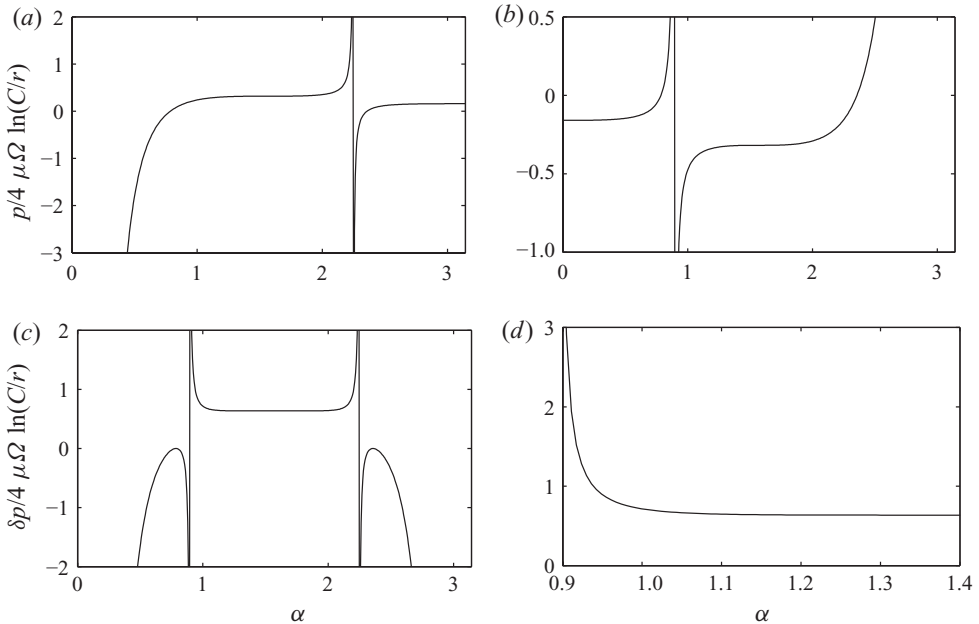


FIGURE 11. (a) Coefficient of the  $\ln(C/r)$  term in the pressure field  $p_u$  on the upper side of the wings; (b) same coefficient in the pressure field  $p_l$  on the lower side; (c, d) coefficient of the  $\ln(C/r)$  term in the pressure jump from the lower to the upper side,  $\delta p = p_u - p_l$ . The range of  $\alpha$  relevant for the insect's flight is between 1 and  $\pi/2$ .

Figures 11(a) and 11(b) show the coefficient of the  $\ln(C/r)$  term in the pressure field on the upper side (3.7) and the lower side (3.8) as a function of the angle  $\alpha$ , and figure 11(c) shows their difference; the flat behaviour in the range of  $\alpha$  between 1 and 2 (about  $57^\circ$ – $104^\circ$ ) is worth noting; a zoomed view is shown in figure 11(d). The fact that near the hinge the pressure is greater on the upper side of the wings than on the lower side for this range of  $\alpha$  is remarkable.

### 3.2. Local similarity solution for sweep

Now consider again what happens in the immediate neighbourhood of the hinge just after the break. The streamfunction consists of three contributions,

$$\psi = \psi_{fl} + \psi_{JH} + \psi_{sw}, \quad (3.9)$$

where  $\psi_{fl}$  is due to rotation of the wings with angular velocity  $\Omega$ ,  $\psi_{JH}$  is the Jeffery–Hamel contribution, and  $\psi_{sw}$  is due to rectilinear motion of the wings during sweep. We assume that the distance between the trailing edges  $d$  is infinitesimally small.

The last two terms in (3.9) appear only after the break, when there is a non-zero flux  $Q$  through the gap between the trailing edges, and the wings move with non-zero outward velocities  $\pm U$ . In this analysis, the boundary conditions are still imposed at two radial lines  $\theta = \alpha$  and  $\theta = -\alpha$ . We assume that the distance between the trailing edges  $d$  is infinitesimally small. Its effect is represented by  $\psi_{JH}$ .

When the radius  $r$  is such that  $d/2 \ll r \ll c$ , the streamfunction (3.9) is a valid local approximation for the solution. Asymptotics for each of the three terms on its right-hand side are given by self-similar solutions of (3.2) with corresponding boundary conditions.



*Contribution due to rotation of the wings* is the same as during fling. This term corresponds to a situation where there is a small gap between the trailing edges, but the flux through it equals zero. When the distance between the trailing edges tends to zero, the streamfunction uniformly converges to the limiting case of fling with no gap between the trailing edges. When approaching the origin at a constant angle  $\theta$ , the streamfunction decreases as  $r^2$ , the vorticity is constant, and the pressure gradient is proportional to  $r^{-1}$ .

*The Jeffery–Hamel sink/source flow* is the flow in a converging channel between two plates. It is driven by a point sink/source of intensity  $Q$  located at the origin and representing the flux between the trailing edges. Here  $Q$  is positive when the fluid is pumped from the upper to the lower side. As we have seen, if the gap  $d(t)$  increases smoothly from zero like  $(t - t_c)^3$ , then we expect the flux  $Q$  through the gap to grow from zero like  $(t - t_c)^5$ . Actually, it grows more slowly now as viscous resistance is included. For example, the numerical simulation in §4.2 indicates  $Q \approx 0.01$  when  $U \approx 0.5$  and  $d \approx 0.1$ .

The wings are fixed, since their motion is taken into account by the two other terms in (3.9). The boundary conditions for the streamfunction are

$$\left. \frac{\partial \psi}{\partial \theta} \right|_{\theta=\alpha} = 0, \quad \left. \frac{\partial \psi}{\partial r} \right|_{\theta=\alpha} = 0, \quad \left. \frac{\partial \psi}{\partial \theta} \right|_{\theta=-\alpha} = 0, \quad \left. \frac{\partial \psi}{\partial r} \right|_{\theta=-\alpha} = 0. \quad (3.10)$$

The low-Reynolds-number limit of this flow was discussed in Moffatt & Duffy (1980) (note that the volume rate is  $2Q$  in the reference). The streamfunction, vorticity and pressure are given by the following relations:

$$\psi_u = -\frac{Q}{2} \frac{\sin 2\theta - 2\theta \cos 2\alpha}{\sin 2\alpha - 2\alpha \cos 2\alpha}, \quad \psi_l = -\frac{Q}{2} \frac{\sin 2\theta + 2(\pi - \theta) \cos 2\alpha}{\sin 2\alpha + 2(\pi - \alpha) \cos 2\alpha}, \quad (3.11)$$

$$\omega_u = -\frac{2Q}{r^2} \frac{\sin 2\theta}{\sin 2\alpha - 2\alpha \cos 2\alpha}, \quad \omega_l = -\frac{2Q}{r^2} \frac{\sin 2\theta}{\sin 2\alpha + 2(\pi - \alpha) \cos 2\alpha}, \quad (3.12)$$

$$p_u = C_u - \frac{2\mu Q}{r^2} \frac{\cos 2\theta}{\sin 2\alpha - 2\alpha \cos 2\alpha}, \quad p_l = C_l - \frac{2\mu Q}{r^2} \frac{\cos 2\theta}{\sin 2\alpha + 2(\pi - \alpha) \cos 2\alpha}. \quad (3.13)$$

Subscripts  $u$  and  $l$  indicate, respectively, the upper  $\theta \in [-\alpha, \alpha]$  and the lower  $\theta \in [\alpha, 2\pi - \alpha]$  sides of the wings.

*Contribution due rectilinear motion of the wings* assumes that the wings move in opposite directions with velocities  $U$  and  $-U$ . The boundary conditions for the streamfunction are then

$$\left. \frac{\partial \psi}{\partial \theta} \right|_{\theta=\alpha} = rU_r, \quad \left. \frac{\partial \psi}{\partial r} \right|_{\theta=\alpha} = U_\theta, \quad \left. \frac{\partial \psi}{\partial \theta} \right|_{\theta=-\alpha} = rU_r, \quad \left. \frac{\partial \psi}{\partial r} \right|_{\theta=-\alpha} = -U_\theta, \quad (3.14)$$

where  $U_r = U \sin \alpha$  and  $U_\theta = U \cos \alpha$ . These boundary conditions suggest the following form for the local similarity solution (see Moffatt 1964):

$$\psi = r f_1(\theta), \quad f_1(\theta) = A \cos \theta + B \sin \theta + C\theta \cos \theta + D\theta \sin \theta. \quad (3.15)$$

The unknown coefficients are obtained by substituting (3.15) into (3.14), yielding the streamfunction

$$\psi_u = -rU \frac{(\alpha \sin 2\alpha - \cos^2 \alpha) \sin \theta + \theta \cos \theta \cos 2\alpha}{\alpha - \sin \alpha \cos \alpha} \quad (3.16)$$

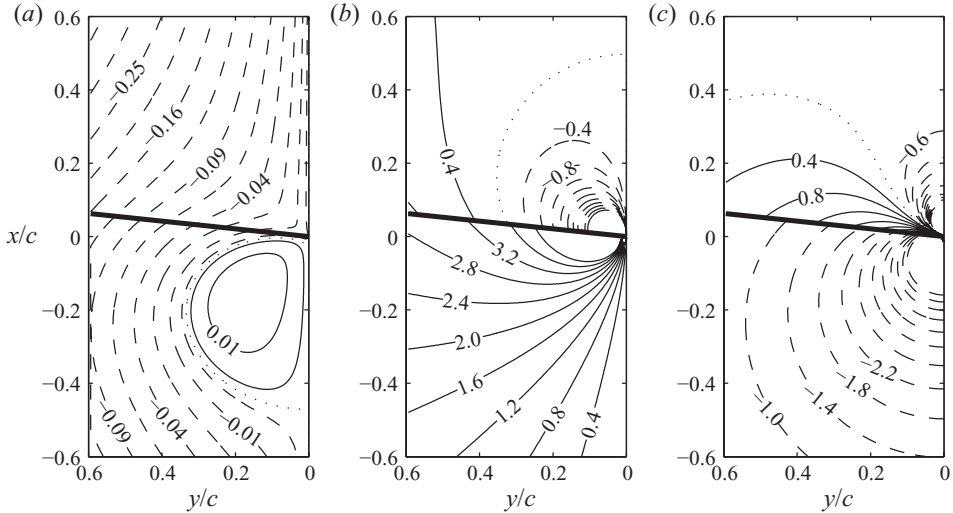


FIGURE 12. Flow during sweep as given by the local similarity solution (3.9) at  $t=1.5$ . (a) Streamlines corresponding to  $\psi \in \pm(0, 0.05^2, 0.1^2, \dots)$ ; (b) isolines of the vorticity drawn with a constant step  $\delta\omega=0.4$ ; (c) isobars drawn with a constant step  $\delta p=0.4$ . Contours of positive and negative values are identified using, respectively, solid and dashed lines. Dots indicate the zero isoline.

on the upper side. Similarly, on the lower side

$$\psi_l = rU \frac{((\pi - \alpha) \sin 2\alpha + \cos^2 \alpha) \sin \theta + (\pi - \theta) \cos \theta \cos 2\alpha}{(\pi - \alpha) + \sin \alpha \cos \alpha}. \quad (3.17)$$

The corresponding relations for the vorticity and the pressure are

$$\omega_u = \frac{2U}{r} \frac{\cos 2\alpha}{\alpha - \sin \alpha \cos \alpha} \sin \theta, \quad \omega_l = -\frac{2U}{r} \frac{\cos 2\alpha}{(\pi - \alpha) + \sin \alpha \cos \alpha} \sin \theta, \quad (3.18)$$

$$p_u = C_u + \frac{2\mu U}{r} \frac{\cos 2\alpha}{\alpha - \sin \alpha \cos \alpha} \cos \theta, \quad p_l = C_l - \frac{2\mu U}{r} \frac{\cos 2\alpha}{(\pi - \alpha) + \sin \alpha \cos \alpha} \cos \theta. \quad (3.19)$$

The two last terms in (3.9) dominate in a sufficiently small neighbourhood around the origin. Strictly speaking, the leading term is  $\psi_{JH}$ , but there is a cutoff at  $r = O(d/2)$ . By noting that  $|\psi_{JH}/\psi_{sw}| = O(Q/Ur) = O(d/r)$ , one can see that  $\psi_{sw}$  is in fact dominant in the range of  $r$  concerned.

Figure 12(a) displays streamlines computed from (3.9) with  $\alpha \approx 1.467$ ,  $\Omega = 1$ ,  $U = 0.088$  and  $Q = 0.01$ , which corresponds to  $t = 1.5$ . The value of  $Q$  is taken from numerical simulations. The streamlines are smooth at  $\theta = \alpha$ , as expected from the no-slip boundary condition. An interesting feature, contrasting with the inviscid case discussed in §2, is the recirculation zone on the lower side. This is obviously not a detached eddy, since the vorticity in figure 12(b) has its maximum on the wing. The isobars, traced in figure 12(c) for  $\mu = 1$ , indicate that sufficiently near the hinge the pressure is negative and that in the limit  $r \rightarrow 0$  it is actually decreasing to  $-\infty$  on both sides of the corner.

The analysis of viscous effects near the hinge is pursued in §4.2, where the local similarity solution is supported by numerical results.

#### 4. Numerical simulations of the viscous clap–fling–sweep mechanism

The numerical simulations presented in this section are intended to supplement the previous theoretical results. First, we are interested in identifying the logarithmic singularity of the pressure during fling. Second, we are interested in the flow in the neighbourhood of the hinge point during the initiation of sweep.

By solving the Navier–Stokes equations, we obtain the flow field around the wings, which contains all the features of the *global* solution, such as the strong vortices generated at the leading edges. However, we seek to compare it with the *local* similarity solution near the hinge point, obtained in the Stokes limit. Therefore, we start by considering the Reynolds number  $Re = 1$ , which is low enough to allow a direct comparison (and for which the local Reynolds number near the hinge is much less than unity), and then we proceed to a more realistic value of the Reynolds number.

Video sequences of the vorticity, streamfunction and pressure visualizations are provided as supplementary data available at [journals.cambridge.org/flm](http://journals.cambridge.org/flm).

##### 4.1. Physical model and numerical method

The model that we use for the numerical simulations is described in more detail in Schneider & Farge (2005) and Kolomenskiy & Schneider (2009). The latter paper contains a validation study for the Lighthill–Weis-Fogh mechanism.

We consider rigid wings moving in a viscous incompressible fluid. The motion of the fluid is governed by the Navier–Stokes equations, completed with a no-slip condition on the solid–fluid interface and a suitable initial condition. As the flow is assumed to be two-dimensional, we use the vorticity–streamfunction formulation of the equations. The no-slip boundary condition is modelled using the volume penalization method (Angot, Bruneau & Fabrie 1999). The wings are assumed to be slightly permeable, and the flow is governed by the penalized vorticity equation

$$\partial_t \omega_\eta + \mathbf{u}_\eta \cdot \nabla \omega_\eta - \nu \nabla^2 \omega_\eta + \nabla \times \left( \frac{\chi}{\eta} (\mathbf{u}_\eta - \mathbf{u}_s) \right) = 0, \quad (4.1)$$

where the penalization parameter  $\eta$  is a small number which controls the permeability of the obstacle. The equation is written for dimensionless parameters and variables. Units are chosen in order to normalize the dimensionless density,  $\rho = 1$ . The vorticity  $\omega_\eta = \nabla \times \mathbf{u}_\eta$  is unknown. The velocity is determined as  $\mathbf{u}_\eta = -\nabla^\perp \psi_\eta$ , with  $\psi_\eta$  being the streamfunction, satisfying

$$-\nabla^2 \psi_\eta = \omega_\eta, \quad (4.2)$$

where  $\nabla^\perp \psi_\eta = (-\partial_y \psi_\eta, \partial_x \psi_\eta)$  denotes the orthogonal gradient of the streamfunction. The parameter  $\nu$  is the kinematic viscosity of the fluid. Equations (4.1) and (4.2) are valid in a computational domain  $A$  which incorporates both the solid wings  $A_s$  and the fluid region  $A_f$  (see figure 13). Geometry and kinematics of the wings are given by the mask function

$$\chi(\mathbf{x}, t) = \begin{cases} 1, & \text{for } \mathbf{x} \in A_s, \\ 0, & \text{for } \mathbf{x} \in A_f, \end{cases} \quad (4.3)$$

and the velocities of the wings  $\mathbf{u}_s(\mathbf{x}, t)$  at each point. Angot *et al.* (1999) rigorously proved that the solution of the penalized Navier–Stokes equation converges to the solution of the Navier–Stokes equation with the no-slip boundary condition when the penalization parameter  $\eta$  tends to zero.

For the spatial discretization of (4.1) and (4.2), we use a classical Fourier pseudo-spectral method in a sufficiently large periodic domain  $A$  (see Canuto *et al.* 1988).

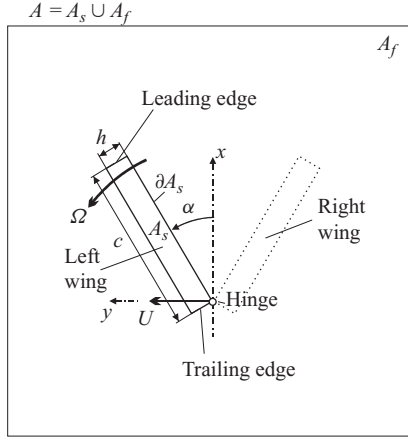


FIGURE 13. Sketch of the computational domain  $A$ , containing the fluid domain  $A_f$ , the solid wings  $A_s$  and their boundary  $\partial A_s$ . Note that the actual thickness-to-chord ratio in the numerical simulations is much smaller ( $h/c = 0.006$ ) than shown in this schematic.

The solution is advanced in time with an adaptive second-order Adams–Bashforth scheme for the nonlinear term, while the viscous term is integrated exactly.

An attractive feature of the volume penalization method is that it allows modelling of moving solid obstacles of complex shape. There is no need for remeshing the computational domain  $A$ , since it remains unchanged in time, and all information about the obstacle shape and its motion is contained in the mask function  $\chi(\mathbf{x}, t)$ , which evolves in space and time. Translation of the obstacle in each direction is implemented by turning the phase of the corresponding Fourier coefficients, and rotation is decomposed into three skewing operations (for details, see Kolomenskiy & Schneider 2009).

The volume penalization method also enables us to compute the fluid forces acting on the wing via volume integration, which is convenient for numerical implementation,

$$\mathbf{F} = \int_A \frac{\chi}{\eta} (\mathbf{u}_\eta - \mathbf{u}_s) dA + hc\dot{\mathbf{U}}_c, \quad (4.4)$$

where  $\dot{\mathbf{U}}_c = d\mathbf{U}_c/dt$  is the acceleration of the centre of volume of the wing.

#### 4.2. Fling–sweep sequence at $Re = 1$

We are interested in identifying the behaviour of the flow near the hinge point, and intend to directly compare the asymptotics derived in §3 with those observed in numerical simulations. For this purpose, we consider a flow at low Reynolds number  $Re = \Omega c^2/\nu = 1$ . The chord length is  $c = 1$ , and the thickness-to-chord ratio is  $h/c = 0.006$ . We use the simplified wing kinematics described in §1 (see also figure 4). The periodic domain size equals  $L_x \times L_y = 10 \times 10$ , it is discretized with  $N_x \times N_y = 8192 \times 8192$  grid points. The penalization parameter is chosen to be  $\eta = 1.5 \times 10^{-5}$  as a good compromise between the precision of the volume penalization method and the computing time.

Figures 14–16 visualize the flow field obtained in this numerical simulation (see also supplementary movie 1). First, we discuss subfigures (a) of these figures, which correspond to time  $t = 1.08$ , just before the break which occurs at  $t_c \approx 1.0805$ . The computed streamlines, shown on the left of figure 14(a), are in qualitative agreement with the asymptotic behaviour given by (3.5), which is shown by a thick dashed line

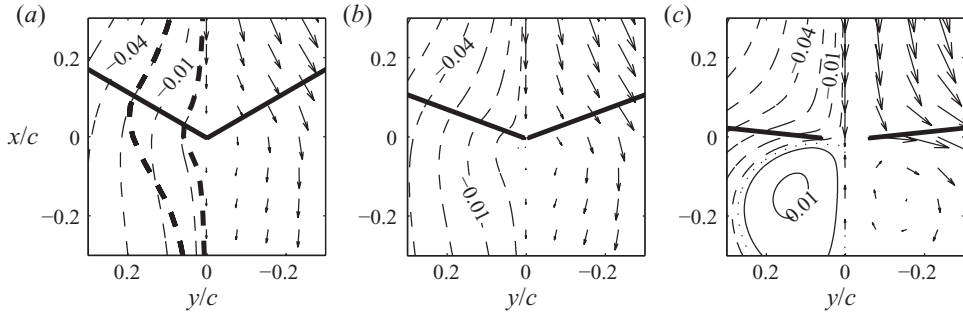


FIGURE 14. Streamlines  $\psi \in \pm(0, 0.05^2, 0.1^2, \dots)$  (left halves of the panels) and velocity vectors (right halves) at three different time instants, (a)  $t = 1.08$ , (b)  $t = 1.25$  and (c)  $t = 1.5$ , as obtained in the numerical simulations at  $Re = 1$ . Thick dashed lines in (a) display streamline  $\psi = -0.0025$  and  $-0.0225$ , as given by the local solution (3.5). Contours of positive and negative values are identified using, respectively, solid and dashed lines. Dots indicate the zero isoline.

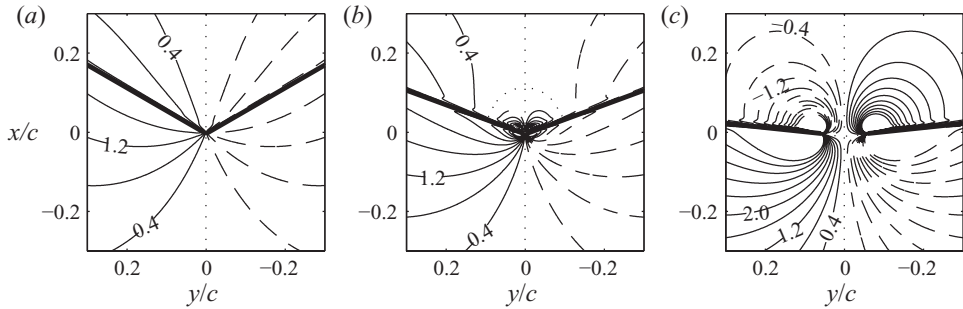


FIGURE 15. Vorticity isolines, drawn with a step  $\delta\omega = 0.4$ . See caption to figure 14 for details.

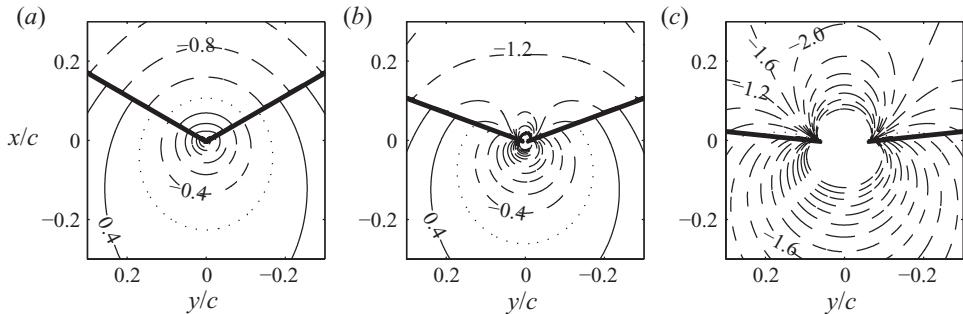


FIGURE 16. Pressure isolines, drawn with a step  $\delta p = 0.4$ . See caption to figure 14 for details.

superimposed on the same figure. The discrepancy below the wing is due to the fact that  $\pi - \alpha$  is close to its critical value  $128.7^\circ$  (see § 3.1). The streamlines pass through the wing, as required by the velocity boundary condition on the interface. The latter is confirmed by the velocity vector plots, and one can also see that the fluid is at rest near the hinge point. At  $r < 0.2$ , the vorticity isolines, plotted in figure 15(a), are almost straight, as expected from (3.6), in which  $\omega$  is proportional to  $\theta$  and does not depend on  $r$ .

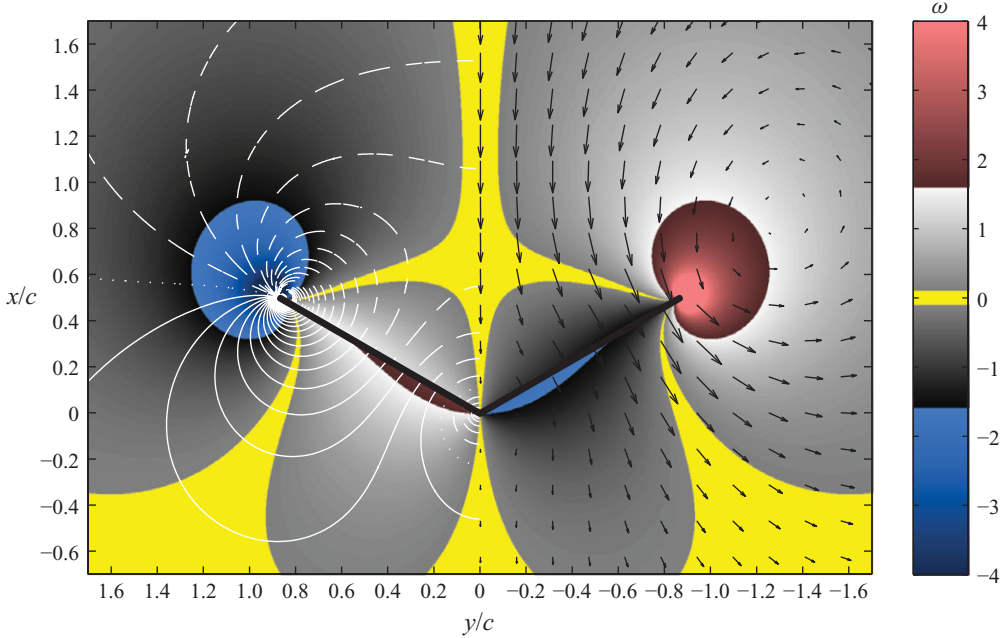


FIGURE 17. (Colour online available at [journals.cambridge.org/FLM](http://journals.cambridge.org/FLM)) Flow during fling at  $Re = 1$ , visualized at  $t = 1.08$ . Colour plot displays the vorticity. Vector plot on the right half of the figure shows the velocity. Contours on the left half are isobars drawn with a constant step  $\delta p = 0.4$ . Their positive, zero and negative values are identified with, respectively, solid, dotted and dashed lines.

The pressure plotted in figure 16(a), indeed, decreases on the lower side and increases on the upper side of the wings, as  $r$  approaches zero. The isolines of the pressure are concentric arcs, in agreement with the local similarity solution (3.7) and (3.8). For  $r < 0.1$  the pressure on the upper side is higher than on the lower side, resulting in a negative contribution to the lift force.

The flow field far from the hinge point also deserves comment (see figure 17 and movie 1). In contrast to the inviscid case of § 2, where all streamlines during fling pass through the wings and form closed loops, in this simulation the streamfunction has its extrema at a certain distance from the wings, although leading-edge vortices remain attached to the wings. This is a viscous effect. A visualization of the streamfunction can be found in movie 1, but the shape of streamlines can also be recognized from the velocity vector plot in figure 17. Near the leading edges, the pressure is positive on the lower side and negative on the upper side, which explains the overall positive lift. Note that when  $Re \rightarrow 0$ , the far-field evolves towards that of a Stokeslet.

Figure 18 displays the pressure gradient along the axis of symmetry of the wings in logarithmic scale. The curves corresponding to the numerical solution of the Navier–Stokes equations suggest that the  $1/r$  asymptotics (3.7) and (3.8) are reasonable, though they deviate when the distance to the hinge point is small enough, i.e. comparable to the thickness of the wings.

A more thorough check of the asymptotic expansion in § 3 would be a comparison with the Stokes flow past infinitesimally thin wings, but of finite chord length. However, our numerical method (as well as real insects) only admits finite thickness, and it can only be decreased with refining spatial discretization. Hence, for validation purposes, we have developed a simple Stokes solver using finite differences, which is

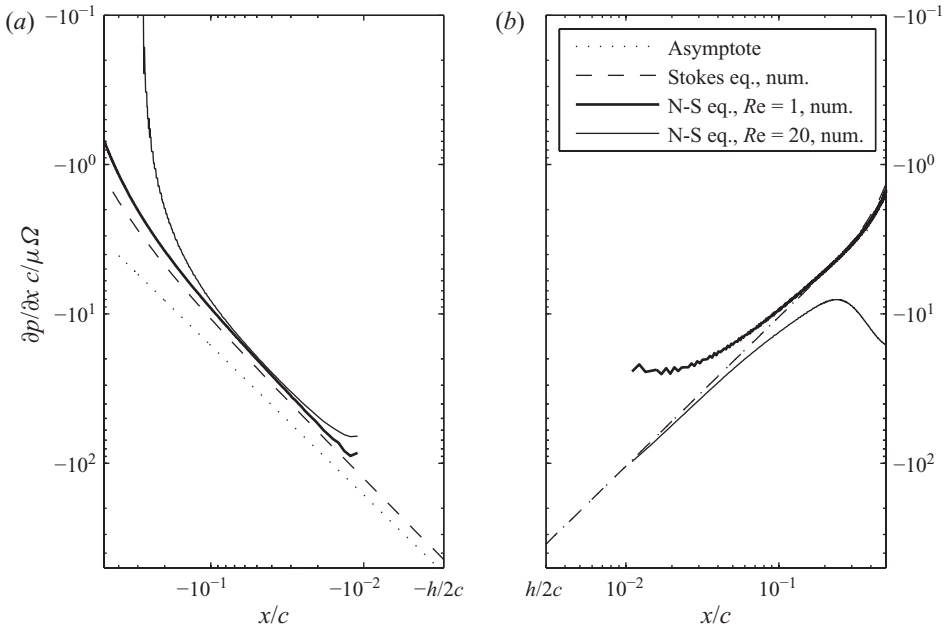


FIGURE 18. Pressure gradient during fling at  $t = t_c$ ,  $\alpha = \pi/3$ , probed on the axis of symmetry of the wings near the hinge. (a) The lower side of the wings and (b) the upper side.

described in Appendix C. The pressure gradient curves thus obtained are shown by dashed lines in figure 18. The  $1/r$  behaviour is well pronounced down to  $|x| = 10^{-3}$ . At large distances from the hinge, the ‘Stokes’ curves are close to those of ‘Navier–Stokes’. At  $|x| \rightarrow 0$ , they approach the similarity asymptotes. However, while the curves perfectly superpose on the upper side ( $x > 0$ ), there is still a noticeable (though decreasing) discrepancy on the lower side ( $x < 0$ ).

This can be explained as follows. The local similarity solution is valid only when the half-angle between the plates is less than  $128.73^\circ$ ; otherwise the flow near the hinge retains a scale dependence on the chord length  $c$  (see Moffatt & Duffy 1980). The solution shown in figure 18 corresponds to  $60^\circ$  on the upper side and  $120^\circ$  on the lower side. Therefore, the global solution may be expected to converge to its asymptote near the hinge more rapidly on the upper side than on the lower side (to substantiate this conjecture, we have also computed the pressure gradient at  $\alpha = 90^\circ$  and observed an equally fast convergence to the local similarity asymptotes on both sides).

We can conclude that the local similarity solution, the numerical solution of the Navier–Stokes equation and the numerical solution of the Stokes equation are in good mutual agreement and prove the logarithmic singularity of pressure at the hinge.

After having identified the singular behaviour of the flow in the proximity of the hinge point, we can proceed to the situation when the wings break apart. At  $t = 1.25$ , the distance between the trailing edges is very small,  $d = 0.0039$ . Both the streamlines and the velocity vectors, shown in figure 14(b), are similar to those at the previous time instant. The difference is visible in figure 14(c) at a later time,  $t = 1.5$ . There are streamlines which pass through the surface of the wings, but one can also see closed loops, exactly as anticipated in §3.2. The velocity equals zero at the centres of these loops, where the streamfunction has local extrema, as well as at the two (instantaneous) stagnation points on the axis of symmetry, one of which is situated between the trailing edges.

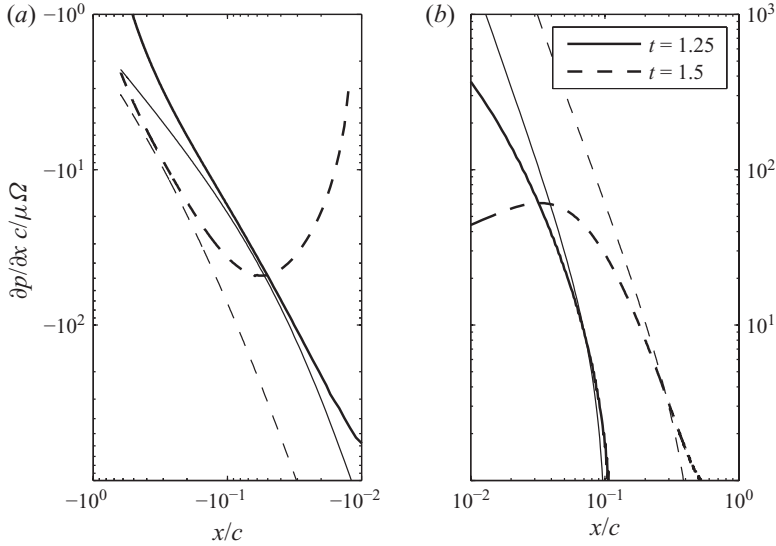


FIGURE 19. Pressure gradient along the axis of symmetry of the wings near the hinge at different time instants  $t = 1.25$  and  $t = 1.5$  during sweep. The numerical results at  $Re = 1$  are shown by thick lines, while thin lines indicate the local similarity solution. (a) The lower side of the wings and (b) the upper side.

Figures 15(b) and 15(c) show the vorticity at the same time instants. The bound vorticity at the trailing edges increases, but the Reynolds number remains too small for vortex shedding. On the upper side of each wing, there is a point at which the vorticity changes sign. This feature is also captured well by the local similarity solution, as seen in figure 12(b). Apparently, it marks the neighbourhood where (3.18) dominates over (3.6).

Let us inspect the pressure fields displayed in figure 16. Note a contrasting difference between  $t = 1.08$  and  $t = 1.25$ . The high positive pressure above the hinge disappears as soon as the wings break apart, and the negative pressure is established around the trailing edges on both sides of the wings. Its figure-of-eight iso-contours are reminiscent of those shown in figure 12(c) for the similarity solution.

In figure 19, one can see the pressure gradient along the axis of symmetry at  $t = 1.25$  and  $t = 1.5$ . It grows approximately like  $|x|^{-2}$  for  $|x| \rightarrow 0$ , which is explained well by  $\partial p_{sw}/\partial x$ , i.e. the gradient of the pressure distribution created by the rectilinear sweep motion (3.19). This behaviour is modified by  $\partial p_{fl}/\partial x$  at large  $|x|$  and by  $\partial p_{JH}/\partial x$  at small  $|x|$ , as well as by other terms neglected in the local analysis.

Now we can explain the flow during the initiation of sweep in a viscous fluid. The streamfunction evolves from  $\psi_{fl}$  to  $\psi_{fl} + \psi_{sw} + \psi_{JH}$ . This transition is continuous, since  $\psi_{sw} + \psi_{JH}$  vanishes when  $t \downarrow t_c$  (everywhere, except at the origin), and important changes of the streamlines are localized in a neighbourhood of radius  $r_\psi \propto U(t)/\Omega$ , where  $\psi_{sw}$  dominates over  $\psi_{fl}$ . This relation can be obtained by equating (3.5) and (3.16) at an arbitrary  $\theta$ . The same is valid for the vorticity, as one can see from (3.6) and (3.18). The pressure behaves differently: the radius  $r_p$ , at which  $p_{sw}$  and  $p_{fl}$  are of the same order of magnitude, evolves nonlinearly such that  $r_p \ln C/r_p \propto U(t)/\Omega$ , where  $C = C(t)$  matches the pressure between the lower and the upper sides. This explains the more rapid change of the pressure compared to other quantities. Note



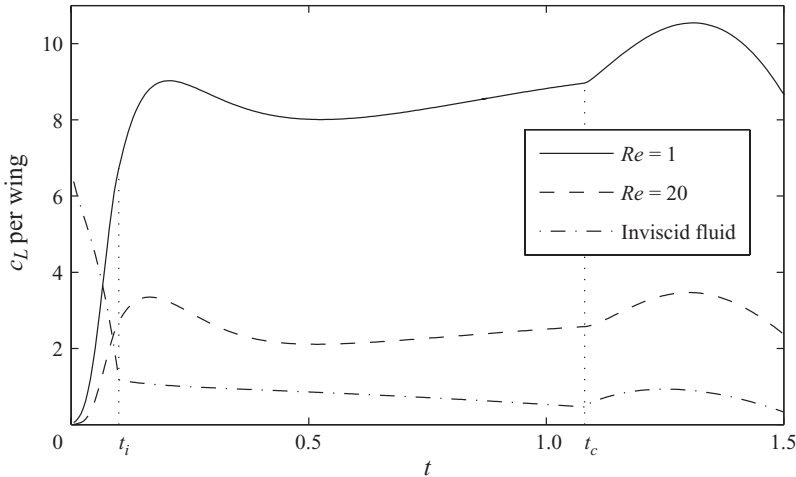


FIGURE 20. Lift coefficient per wing obtained in numerical simulations of viscous fluid flows at  $Re = 1$  (solid line) and  $Re = 20$  (dashed line). Lift coefficient in an inviscid fluid is also shown for comparison (dash-dotted).

that in a viscous fluid the pressure evolves continuously in time, in contrast to the instantaneous redistribution that occurs in an inviscid fluid.

To supplement the description of the flow, the time history of the lift coefficient per wing,  $c_L = 2L/\rho\Omega^2c^3$ , is traced in figure 20. The unusually large values of  $c_L$  are explained by the low Reynolds number. After a rapid growth at the initial phase of the ‘fling’, associated with a strong vorticity production,  $c_L$  slowly increases when the angular velocity is kept constant, until it starts increasing more rapidly when the wings break apart. It is noteworthy that the change of the slope at  $t = t_c$  is qualitatively the same in both the inviscid and the viscous fluids, and reflects the linearly increasing acceleration of the wings during sweep,  $\dot{U} \propto (t - t_c)$ .

The increase in  $c_L$  during fling in a viscous fluid is related to the leading-edge vortices (Spedding & Maxworthy 1986). At  $Re = 1$ , they remain attached to the wings, and the vorticity only propagates by diffusion. In this connection, it is interesting to note that, after an initial transient, the slope of the  $c_L$  curve is approximately the same as it would be at a larger Reynolds number  $Re = 20$ , where inertial effects are important and the leading-edge vortices are shed from the wings.

#### 4.3. Fling–sweep sequence at $Re = 20$

The unit Reynolds number in the previous section was chosen in order to make a clear evidence of the viscous local effects near the trailing edges. Real insects, however, operate in the range of Reynolds numbers where inertial forces are more important. For *E. formosa*, Weis-Fogh (1973) measured the chord length  $c \approx 0.3$  mm, the stroke-arc-to-wing-chord ratio  $\Lambda \approx 4$  and the flapping frequency  $f \approx 400$  s<sup>-1</sup>. In nature, these parameters appreciably vary, and the motion of the wings is complex, but  $Re = 20$  seems to be a representative value. Let us therefore consider this regime. The numerical simulation was performed with the penalization parameter  $\eta = 10^{-4}$ , while the other parameters were the same as in §4.2.

Figure 21 displays the vorticity field at  $t = 1.08$ , with the velocity vectors and isobars superimposed on it. It shows vortex shedding from the leading edges. However, the cores of these vortices remain near the wings, and they are shifted towards the upper surfaces, which creates a larger depression above the wings (see also movie 2). Another

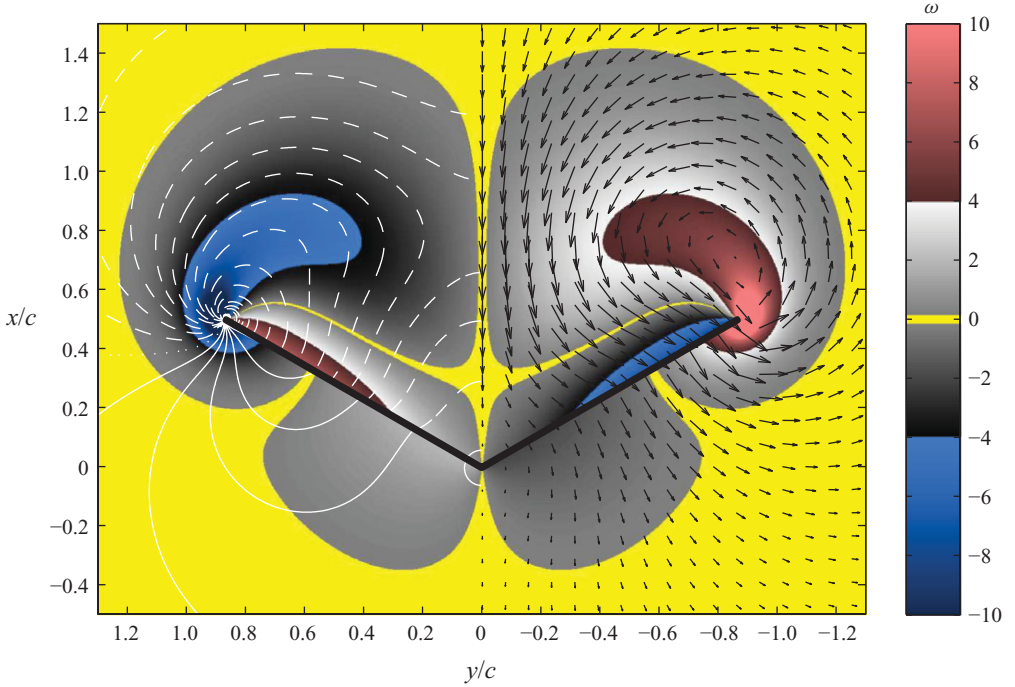


FIGURE 21. (Colour online) Flow during fling at  $Re=20$ , visualized at  $t=1.08$ . Colour plot displays the vorticity. Vector plot on the right half of the figure shows the velocity. Contours on the left half are isobars drawn with a constant step  $\delta p=0.125$ . Their positive, zero and negative values are identified with, respectively, solid, dotted and dashed lines.

outcome is a strong downward jet between the two vortices, which hits the interior of the hinge and thus modifies the flow there.

Nevertheless, as soon as a sufficiently small neighbourhood of the hinge is viewed, the local effects overcome the influence of the far-field. This is evidenced by the vorticity being virtually independent of  $r$  when  $r < 0.1$ , and by the circular isobars in the hinge vicinity. The region of negative pressure just below the hinge is very small; therefore, it is not seen in figure 21. However, figure 18 confirms that, even at  $Re=20$ , the pressure decreases logarithmically when approaching the hinge from the lower side.

The lift coefficient, shown by a dashed line in figure 20, is two to four times smaller than at  $Re=1$ . This drop is typical for the range of  $Re$  in question. Meanwhile, the main trends are unchanged: after an initial transient,  $c_L$  slowly grows during fling, then increases and falls off during sweep. At all stages, except at the very beginning of the process, the lift coefficient remains far greater than that generated in an ideal fluid. This was stated in earlier studies, but, to our knowledge, no exact quantitative comparison between the two cases has been made in terms of the lift coefficient.

#### 4.4. Clap–fling–sweep sequence at $Re=20$

In §§4.2 and 4.3, we assumed that the fling motion starts in a fluid at rest. This assumption may be true for the first downstroke, but all subsequent downstrokes are preceded by upstrokes. Thus, fling is usually preceded by clap (see figure 3), and one may question how this situation modifies the flow described previously.

We performed a numerical simulation of the clap–fling–sweep sequence at  $Re=20$ . During clap,  $\alpha=t$  and  $d/2=-t-\sin t$ , as shown by dashed lines in figure 4. The

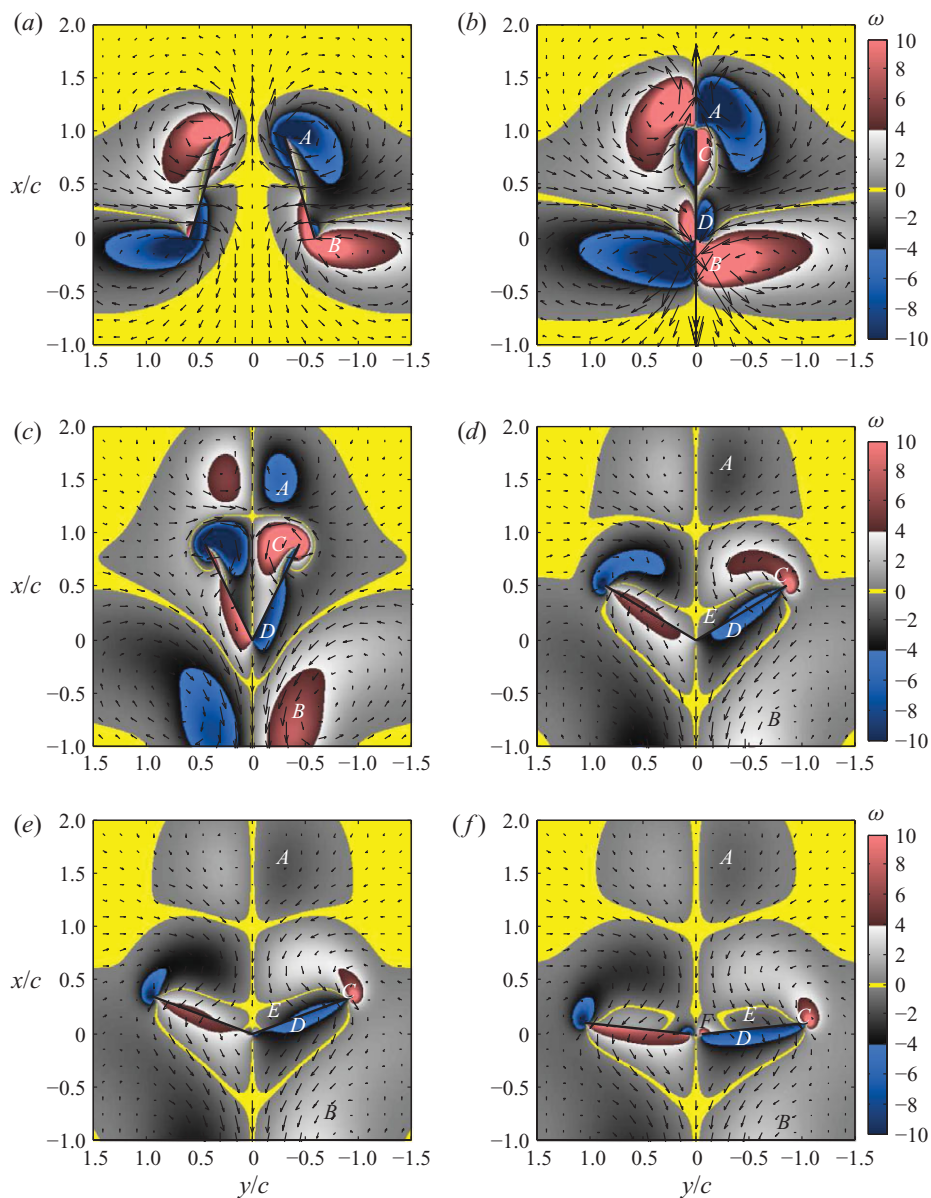


FIGURE 22. (Colour online) Vorticity (colour plots) and velocity (vector plots) during clap–fling–sweep at  $Re = 20$ . Time instants are (a)  $t = -0.3$ , (b)  $t = 0$ , (c)  $t = 0.5$ , (d)  $t = 1.08$ , (e)  $t = 1.25$  and (f)  $t = 1.5$ . Letters A to F denote pairs of vortices generated by the two wings.

simulation starts at  $t = -1.5$ . Other parameters are the same as in §4.3. Note that clap is not a mirror image of fling. It is faster and at larger angle of incidence. The wings impulsively stop when they touch each other. These features are inspired by observations of Weis-Fogh (1973), but the clap motion discussed here is, of course, a major idealization of the real process.

Figure 22 displays the flow field at six successive time instants. Figure 22(a) shows clap at  $t = -0.3$ , when the wings approach each other. Two vortex pairs (denoted by letters A and B in the figure) are generated at the leading and trailing edges, and

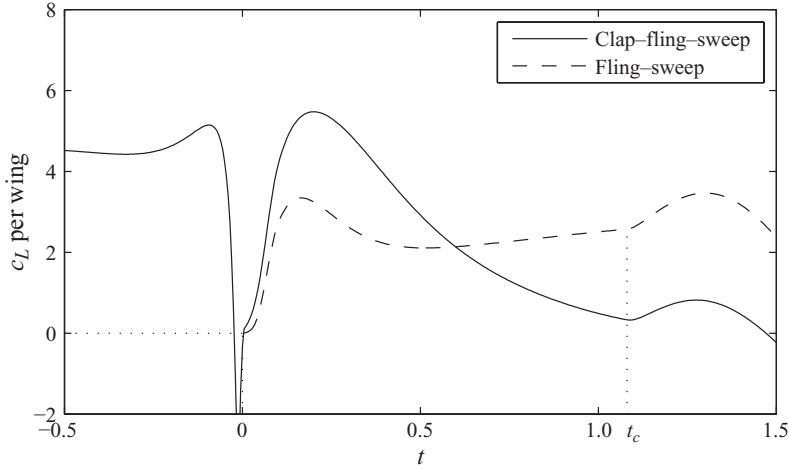


FIGURE 23. Lift coefficient per wing during the clap–fling–sweep process (solid line) and during the fling–sweep sequence only, when the wings are initially clapped and start in a fluid at rest (dashed line, also see figure 20). The Reynolds number is  $Re = 20$ .

they are associated with two vertical jets in opposite directions. The vertical velocity is the largest at  $t = 0$ , the moment when the wings are fully clapped (figure 22*b*), and the downward jet is stronger than the upward. Vortex pairs *A* and *B* then detach and propagate upwards and downwards, respectively. Their interaction with the wings forms vortex pairs *C* and *D*, which are, respectively, opposite to *A* and *B*. During fling (figures 22*c* and 22*d*), vortices *C* evolve to become the leading-edge vortices, as seen in figure 21, but in the present case they are significantly weaker due to interaction with vortices *A*. On the contrary, vortices *D* are stronger in this numerical simulation. Vortices *E* are almost unaffected by the presence of clap. Similarly, vortices *F* during sweep (figures 22*e* and 22*f*) are explained well by the local analysis presented in §3.2.

Time history of the lift coefficient  $c_L$  is shown in figure 23. During clap, the lift coefficient is positive, until at the end when it rapidly drops below zero, because larger suction force is exerted on the trailing edges than on the leading edges. This behaviour is in agreement with experimental observations of Lehmann, Sane & Dickinson (2005). Numerical simulations of Sun & Yu (2003) and Miller & Peskin (2005) exhibited similar trends, but with a broader negative peak and different minimum and maximum values of  $c_L$ , because the kinematics were different.

Positive lift coefficient re-establishes during fling, and its peak is significantly larger compared to the value obtained without clap. However, during the last part of the fling, the lift coefficient decreases, and it almost vanishes at the moment of break  $t_c$ . During sweep, it regains and then drops again, in a manner consistent with the previous results.

To conclude, the flow near the trailing edges during fling and sweep is not very sensitive to the initial condition. But the flow near the leading edges is. For this reason, clap has a strong influence on the lift coefficient. Strong interdependence between the lift coefficient and the wake suggests, as a further step, making a numerical simulation of wings performing several full strokes. However, three-dimensionality of the flow becomes essential at this point (cf. Maxworthy 1979, 2007). An analysis of the three-dimensional effects is beyond the scope of this paper, and will be reported elsewhere.

## 5. Conclusions

To summarize the results of our analytical and numerical study of the Lighthill–Weis-Fogh mechanism, let us draw the following conclusions.

(i) Lighthill’s two-dimensional inviscid scenario is correct to the extent that circulation (equal and opposite around the two wings) can be generated in an inviscid fluid and that this circulation appears when a solid body immersed in the fluid breaks into two pieces (when fling gives way to sweep). Bound vortex sheets produced during fling are still carried by the just-separated wings. This is associated with a continuous time evolution of the velocity everywhere in the fluid, provided the linear and angular velocities of the wings are continuous.

Kelvin’s theorem requires circulations around each wing to be constant during sweep. This implies a discontinuity in the time derivative of the bound vorticity, even if the linear and angular accelerations of the wings are continuous (unless when the incidence angle of the wings at the moment of break  $\alpha_c = \pi/2$ ). In correspondence with this, the pressure field in the fluid changes instantaneously when the break occurs.

In a general situation, the lift is non-zero. Before the break, it is associated with the changing shape of the body (such as the force acting on an accelerating body in an inviscid fluid, this is a ‘virtual mass’ effect). After the break, it is associated with a combination of this type of ‘acceleration force’ and the Magnus force  $\rho U \Gamma$  on each wing, which ultimately dominates.

We should note that Lighthill’s description of the flow during ‘fling’ as being predominantly a sink-type flow is clearly erroneous. The far-field is a dipole flow during both fling and sweep, and this is quite important because the dipole strength is closely related to the momentum stored in the fluid, and the rate of change of this momentum is in turn related to the lift.

(ii) Viscous effects are important not only in relation to vortex shedding at the leading edges of the wings (as previously recognized). In particular, viscous stresses control the build-up of flow through the opening gap between the wings just after the break.

In profound contrast to the inviscid case, and to Lighthill’s assumption of a negligible pressure jump at the hinge point just before the break, the pressure has a logarithmic singularity there, it is positive above, and negative below. After the break, the local flow is dominated by the outward translational motion of the wings, and the pressure becomes negative above as well as below. Unlike in the inviscid situation, no immediate redistribution of pressure occurs, except just at the hinge point, at which the infinite pressure jump has to disappear when the wings separate.

Near the trailing edges, the local Reynolds number immediately after the break is very low, and the flow there is described well by similarity solutions of the Stokes equation. In this situation, no trailing-edge vortex shedding occurs, and the Wagner effect is not present.

The lift generated in a viscous fluid is much greater than in an inviscid fluid. It grows during fling, in contrast to the inviscid case. During sweep, the lift evolves similarly in both cases, essentially due to the acceleration reaction. The average lift coefficient at  $Re = 1$  is 8.3 times larger than in the inviscid case. At  $Re = 20$ , it is 2.5 times larger.

(iii) We restrict the scope of this paper to the two-dimensional approximation. Three-dimensionality of the flow in a real situation will be addressed elsewhere.

D.K., K.S. and M.F. thank Trinity College, Cambridge, for hospitality. M.F. is also grateful to the Wissenschaftskolleg zu Berlin for hospitality and thanks R. Page and H. Wolf for fruitful discussions about *E. formosa* while she was there. D.K. thanks T. Maxworthy and J. Wang for useful discussions, and D. Fougère for computational

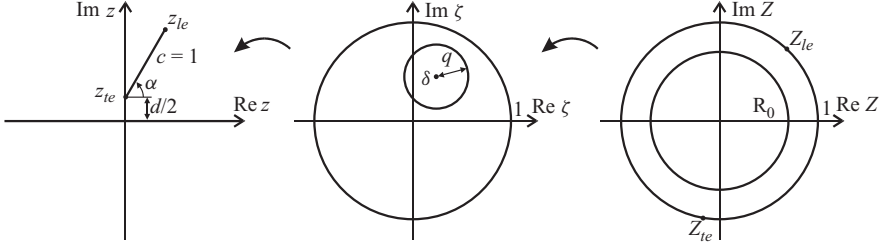


FIGURE 24. Schematic illustration of the conformal mapping.

assistance. Some numerical simulations were conducted using NEC SX-8 computer at IDRIS, project 81664. D.K. and K.S. acknowledge financial support from the Deutsch-Französische Hochschule, project ‘S-GRK-ED-04-05’

Supplementary movies are available at [journals.cambridge.org/flm](http://journals.cambridge.org/flm).

### Appendix A. A method for calculating potential flow during sweep

Consistent with Lighthill’s model for fling, we consider a single wing moving away from an infinite plane boundary. The physical domain is a half-plane with an embedded slit; this can be obtained by conformal mapping from an annulus, as shown by Crowdy (2007).

We use a superposition of two mappings,  $z = z(\zeta(Z))$ , illustrated in figure 24. The following formula can be used for mapping from a domain bounded by two non-concentric circles to the physical domain (cf. Appendix B in Crowdy 2007):

$$z(\zeta) = iC_1 \frac{\omega(\zeta, 1)}{\omega(\zeta, -1)} + C_2, \quad (\text{A } 1)$$

where  $C_1$  and  $C_2$  are constants, and  $\omega(\zeta, \gamma)$  is the Schottky–Klein prime function. Crowdy & Marshall (2007) developed an efficient algorithm based on the Fourier–Laurent expansion and implemented it in a Matlab code ([www2.imperial.ac.uk/~dgcrowdy/SKPrime](http://www2.imperial.ac.uk/~dgcrowdy/SKPrime)) which we use in the present work. In a doubly connected domain, the Schottky–Klein prime function is generated by only one Möbius map,

$$z = \delta + \frac{q^2 \zeta}{1 - \bar{\delta} \zeta}, \quad (\text{A } 2)$$

where  $\delta$  is the centre of the inner circle and  $q$  is its radius. The four parameters  $C_1$ ,  $C_2$ ,  $\delta$  and  $q$  can be chosen to ensure the desired angle of incidence  $\alpha$  and chord length  $c$ , and to place the trailing edge at the point  $id/2$ . The values of  $\delta$  and  $q$  are found by an iterative process. Note that Crowdy (2009) proposes a convenient formula that requires iteration for only one parameter. The mapping from the non-concentric circles to the concentric circles is given by

$$\zeta = \frac{\delta Z - bR_0}{|\delta| bZ - R_0}, \quad (\text{A } 3)$$

where

$$b = \frac{1 + x_1 x_2 + \sqrt{(1 - x_1^2)(1 - x_2^2)}}{x_1 + x_2}, \quad R_0 = \frac{ax_2 - 1}{x_2 - a}, \quad x_1 = |\delta| + q, \quad x_2 = |\delta| - q. \quad (\text{A } 4)$$

Now, the exterior boundary is the unit circle, which maps to the wing, and the interior is a circle of radius  $R_0$ , which maps to the  $x$ -axis.

The Jacobian of the mapping is

$$\frac{dz}{dZ} = \frac{dz}{d\zeta} \frac{d\zeta}{dZ}, \quad (\text{A } 5)$$

where

$$\frac{dz}{d\zeta} = iC_1 \frac{\omega_\zeta(\zeta, 1)\omega(\zeta, -1) - \omega_\zeta(\zeta, -1)\omega(\zeta, 1)}{\omega^2(\zeta, -1)}, \quad (\text{A } 6)$$

$$\frac{d\zeta}{dZ} = \frac{\delta}{|\delta|} \frac{R_0(b^2 - 1)}{(bZ - R_0)^2}, \quad (\text{A } 7)$$

and the derivatives  $\omega_\zeta$  are again evaluated using the Fourier–Laurent expansion.

While  $z(Z)$  is known explicitly, evaluation of its inverse  $Z(z)$  is more costly since it requires solving an equation. This must be done for the leading edge,  $z_{le}$ , and the trailing edge,  $z_{te}$ , in order to fix the values of parameters  $C_1$  and  $C_2$ . We evaluate  $l(\theta) = |z(e^{i\theta})|$  at a number of equidistant points, and then solve  $dl/d\theta = 0$ . This gives two angles  $\theta_{le}$  and  $\theta_{te}$ , which respectively maximize and minimize the distance  $l(\theta)$ . Note further that  $\zeta = 1$  maps to  $C_2$ , and  $\zeta = -1$  maps to the point at infinity in the physical domain.

Knowing the conformal mapping, the problem reduces to finding the values of the complex potential  $w = \phi + i\psi$  inside the annular domain,

$$\left. \begin{aligned} \nabla^2 w &= 0, \\ \text{Im } w &= 0 \quad \text{on } |Z| = R_0, \\ \text{Im } w &= \psi_{te} - \Omega l_{te}^2/2 - U l_{te} \cos \alpha \quad \text{on } |Z| = 1, \end{aligned} \right\} \quad (\text{A } 8)$$

where  $\Omega$  is the angular velocity of the wing,  $U$  is the velocity of sweep,  $\alpha$  is the angle of incidence, and  $l_{te} = |z(e^{i\theta}) - z_{te}|$ . The value of the streamfunction at the trailing edge  $\psi_{te}$  determines the mean value of  $\psi$  along the unit circle, and hence the circulation around the wing,

$$\Gamma = -\frac{1}{\ln R_0} \int_0^{2\pi} (\psi_{te} - \Omega l_{te}^2/2 - U l_{te} \cos \alpha) d\theta. \quad (\text{A } 9)$$

The solution of (A 8) may be written as

$$w = \frac{\Gamma}{2\pi i} \ln \frac{R_0}{Z} - \frac{1}{2\pi i} \int_0^{2\pi} (\psi_{te0} - \Omega l_{te}^2/2 - U l_{te} \cos \alpha) \left( 1 - 2 \frac{Z}{e^{i\theta}} \frac{\omega_\zeta(Z/e^{i\theta}, 1)}{\omega(Z/e^{i\theta}, 1)} \right) d\theta + C. \quad (\text{A } 10)$$

Here, the first term is the complex potential of a point vortex of strength  $\Gamma$  placed at the origin. The second term corresponds to the flow with zero circulation around the wing, given by the Villat formula (see Akhiezer 1990; Crowdy, Surana & Yick 2007), which only admits the value of  $\psi_{te0}$  determined from the compatibility condition

$$\psi_{te0} = \frac{1}{2\pi} \int_0^{2\pi} (\Omega l_{te}^2/2 + U l_{te} \cos \alpha) d\theta. \quad (\text{A } 11)$$

The Schottky–Klein function  $\omega$  is generated this time by the map  $z = R_0^2 \zeta$ . Here  $C$  is a real constant chosen such that  $\phi$  vanishes at infinity.

The complex velocity in the physical domain is  $u - iv = dw/dz$ ,  $= dw/dZ dZ/dz$ , where

$$\frac{dw}{dZ} = -\frac{\Gamma}{2\pi i} \frac{1}{Z} + \frac{1}{\pi i} \int_0^{2\pi} (\psi_{te0} - \Omega l_{te}^2/2 - U l_{te} \cos \alpha) \frac{1}{e^{i\theta}} \left( \frac{\omega_\zeta}{\omega} + \frac{Z}{e^{i\theta}} \frac{\omega_{\zeta\zeta} \omega - \omega_\zeta^2}{\omega^2} \right) d\theta \quad (\text{A } 12)$$

is the complex velocity in the annular domain.

The complex potential (A 10) and the complex velocity (A 12) are only functions of instantaneous values of  $\alpha$ ,  $d/2$ ,  $\Omega$  and  $U$ . The pressure  $p$  is given by (2.13) and, obviously, depends on accelerations via the time derivative of the potential. It is difficult to obtain an explicit formula, because there is no obvious way to explicitly relate the mapping parameters  $q(t)$  and  $\delta(t)$  to the physical parameters  $\alpha(t)$ ,  $d(t)/2$  and  $c$ . The unsteady pressure component is therefore evaluated numerically using a centred fourth-order finite-difference scheme,

$$-\rho \frac{\partial \phi}{\partial t}(z, t) = -\frac{\rho}{\Delta t} \sum_{k=-2}^2 b_k \phi(z, t + k\Delta t) + O(\Delta t^4), \quad (\text{A } 13)$$

where  $b = (1/12, -2/3, 0, 2/3, -1/12)$ .

The total forces on the wing are also evaluated numerically. Integrals in (2.24) are taken over a circle in the annular domain,  $Z = R_S e^{-i\theta}$ , where  $R_S$  is any number between  $R_0$  and 1. Then  $dZ = iZ d\theta$ , and (2.24) is discretized in space using the periodic trapezoid rule with integration points  $\theta_j = 2\pi j/n$ ,  $j = 1, \dots, n$ . Note that counterclockwise paths in the annular domain become clockwise when mapped in the physical domain, and the integrals change sign. Hence, a discrete counterpart of (2.24) is obtained,

$$F \approx \rho \frac{2\pi}{n} \left\{ \frac{1}{2} \sum_{j=1}^n \left[ \left( \frac{dw}{dZ} \right)^2 \left( \frac{dz}{dZ} \right)^{-1} Z \right]_{j0} + \frac{1}{\Delta t} \sum_{k=-2}^2 b_k \sum_{j=1}^n \left[ z \frac{dw}{dZ} Z \right]_{jk} \right\}, \quad (\text{A } 14)$$

where  $z$ ,  $dz/dZ$  and  $dw/dZ$  are given, respectively, by (A 1), (A 5) and (A 12). Subscripts  $k$  and  $j$  denote quantities evaluated at time  $t + k\Delta t$  and at azimuthal point  $\theta_j$ . This scheme is spectral in space and fourth-order accurate in time.

## Appendix B. On the lift coefficient of the inviscid mechanism

To supplement the discussion in §2.4, here we examine the lift coefficient of the inviscid Lighthill–Weiss–Fogh mechanism with different kinematics. First, let us consider the motion proposed by Miller & Peskin (2005). Between  $t = 0$  and  $t = 1.74$ , the wings rotate with angular speed

$$\Omega(t) = \frac{1}{2} \Omega_{rot} \left[ 1 - \cos \left( 2\pi \frac{t - t_{turn}}{\Delta t_{rot}} \right) \right], \quad (\text{B } 1)$$

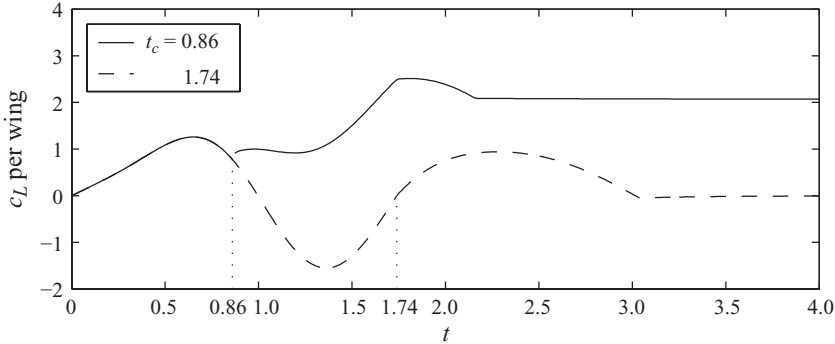
where  $\Omega_{rot} = 2\Delta\theta U_{max}/\Delta t_{rot} c$ ,  $\Delta\theta = \pi/4$ ,  $\Delta t_{rot} = 1.74$  and  $t_{turn} = 0$ . The translational motion begins at  $t_c = 0.86$ . The wings start sweeping apart with increasing speed

$$U(t) = \frac{1}{2} U_{max} \left[ 1 + \cos \left( \pi + \pi \frac{t - t_c}{\Delta t_{accel}} \right) \right], \quad (\text{B } 2)$$

where  $\Delta t_{accel} = 1.3$ . After  $t = t_c + \Delta t_{accel}$ , the speed remains equal to  $U_{max} = 1$ .

The lift coefficient is shown in figure 25 by a solid line. During fling, the maximum of  $c_L$  equals 1.26, i.e. slightly more than a half of its value at  $Re = 128$  reported



FIGURE 25. Lift coefficient per wing with  $\Omega$  and  $U$  as in (B1) and (B2).

by Miller & Peskin (2005). There is a noticeable discontinuity at  $t_c$ . The maximum during sweep is reached approximately at  $t=1.74$ , when the wings stop rotating. This corresponds well to the viscous case. By coincidence,  $c_{Lmax}=2.51$  also agrees well with the numerical simulation at  $Re=128$ . At  $t=2.16$ , the acceleration reaction disappears, and the change of the slope of  $c_L(t)$  reflects the corresponding change of  $\dot{U}$ . Then, the lift remains equal to  $\rho\Gamma U$ , and there is no visible interference between the wings. The corresponding  $c_L=2.07$  is much larger than the real value in a viscous fluid.

The dashed line in figure 25 corresponds to (B1)–(B2) with  $t_c=1.74$ . Hence, the wings fully stop at  $t_c$ , and then start translating. Their circulation  $\Gamma$  equals zero at the moment of break and remains unchanged in the subsequent motion. Of course,  $c_L(t_c)=0$ . Moreover, the integral  $\int_0^{t_c} c_L dt=0$ , i.e. no net lift is generated during fling. There is a positive contribution during sweep, but only due to the acceleration reaction. Obviously, this contribution also cancels out if the wings reverse and clap.

### Appendix C. Finite-difference solution of the Stokes equation

This appendix describes the Stokes solver which was developed to validate the similarity solution for fling, as mentioned in §4.

Let the streamfunction  $\psi$  satisfy the Stokes equation (3.2) with  $\psi = \Omega r^2/2$ ,  $\partial\psi/\partial n=0$  on the wings. The computational domain is circular, with its centre at the hinge point. The radius  $R$  of its outer boundary is large (but limited with the maximum grid size) and the radius of its inner boundary is zero. This domain is parametrized with polar coordinates  $(r, \theta)$  and (3.2) is solved in it with the following boundary conditions:

- (i)  $\psi = \Phi_1$ ,  $\partial\psi/\partial r = \Phi_2$  on the outer circular boundary (assuming  $\Phi_1 = \Phi_2 = 0$ );
- (ii)  $\psi = 0$ ,  $\partial\psi/\partial r = 0$  on the inner degenerate boundary and
- (iii)  $\psi = \Omega r^2/2$ ,  $\partial\psi/\partial\theta = 0$  on the wings.

The streamfunction of the flow due to flapping wings in a Stokesian fluid grows indefinitely large at large distances from the wings. However, the boundary conditions for the numerical solution are prescribed at a finite distance from the wings, and the flow due to a two-dimensional Stokeslet could provide adequate values of  $\psi$  and  $\partial\psi/\partial n$  on the outer boundary (see Batchelor 2000). Numerical experiments show that these conditions are unimportant if the outer boundary is sufficiently far.

The Laplace operator in polar coordinates reads as

$$\nabla^2 = \frac{\partial^2}{\partial r^2} + r^{-1} \frac{\partial}{\partial r} + r^{-2} \frac{\partial^2}{\partial \theta^2}, \quad (\text{C1})$$

and the Stokes equation (3.2) can be rewritten as

$$\left( \frac{\partial^2}{\partial r^2} + r^{-1} \frac{\partial}{\partial r} \right)^2 \psi + \left( 2r^{-2} \frac{\partial^2}{\partial r^2} - 2r^{-3} \frac{\partial}{\partial r} + 4r^{-4} \right) \frac{\partial^2 \psi}{\partial \theta^2} + r^{-4} \frac{\partial^4 \psi}{\partial \theta^4} = 0. \quad (\text{C2})$$

The streamfunction is sought in the form  $\psi = \psi_1 + \psi_2$ . The contribution  $\psi_2$  is an arbitrary function which verifies non-homogeneous boundary conditions. In contrast, the contribution  $\psi_1$  equals zero on the boundaries, and in the interior it is determined from the equation

$$\nabla^4 \psi_1 = -\nabla^4 \psi_2. \quad (\text{C3})$$

Thus, the problem reduces to solving a bi-harmonic equation with non-vanishing right-hand side and homogeneous boundary conditions.

Derivatives in  $\theta$  are approximated on a uniform grid with finite differences as follows.

(i) Second derivatives are computed with a central second-order scheme (in what follows,  $f$  is any given function)

$$\frac{\partial^2 f}{\partial \theta^2}(r_i, \theta_j) \approx \frac{f_{i,j+1} - 2f_{i,j} + f_{i,j-1}}{\Delta \theta^2}. \quad (\text{C4})$$

(ii) Fourth derivatives are obtained everywhere, except at the points next to the wings, by applying twice the second derivative operator. At the nearest points on each side of the wings, the following scheme is used:

$$\frac{\partial^4 \psi}{\partial \theta^4}(r_i, \theta_{j_w-1}) \approx -\frac{2}{3} \frac{11\psi_{i,j_w} - 18\psi_{i,j_w-1} + 9\psi_{i,j_w-2} - 2\psi_{i,j_w-3}}{\Delta \theta^4}, \quad (\text{C5})$$

$$\frac{\partial^4 \psi}{\partial \theta^4}(r_i, \theta_{j_w+1}) \approx -\frac{2}{3} \frac{11\psi_{i,j_w} - 18\psi_{i,j_w+1} + 9\psi_{i,j_w+2} - 2\psi_{i,j_w+3}}{\Delta \theta^4}, \quad (\text{C6})$$

where  $j_w = j_{w \text{ left}}$  (or  $j_w = j_{w \text{ right}}$ ) is the index of the grid line which coincides with the left (or right) wing centreline. By construction of the interpolant, this scheme guarantees that the first derivative in  $\theta$  equals zero on the wings.

Derivatives in  $r$  are evaluated using a Chebyshev spectral collocation method (see e.g. Canuto *et al.* 1988). The grid points cluster near the boundaries,  $r_i = R(1 - \cos(i\pi/N))/2$ ,  $i = 0, \dots, N$ . This property is useful for our purpose of identifying the asymptotic behaviour at  $r \rightarrow 0$ .

Discretization of (C3) results in a linear system of equations which is solved for  $\psi_1$  at interior points. After the streamfunction  $\psi$  is found, the vorticity is calculated as  $\omega = -\nabla^2 \psi$  using the same numerical schemes. The pressure is computed from the relations

$$\frac{\partial p}{\partial x} = -\frac{\partial \omega}{\partial y}, \quad \frac{\partial p}{\partial y} = \frac{\partial \omega}{\partial x}. \quad (\text{C7})$$

For that purpose, the vorticity is interpolated to a Cartesian grid in  $x$ - $y$  coordinates and its derivatives are calculated with central differences of second order. Then, the pressure at every point is computed as a contour integral, with the integration contours chosen not to cross the wing.

This numerical method, despite being imperfect, is good enough to capture the essential features of the flow.

## REFERENCES

- AKHIEZER, N. I. 1990 *Elements of the Theory of Elliptic Functions, Translations of Mathematical Monographs*, vol. 79. American Mathematical Society (*Elementy teorii ellipticheskikh funktsij*, Nauka, 1970).
- ANGOT, P., BRUNEAU, C.-H. & FABRIE, P. 1999 A penalisation method to take into account obstacles in viscous flows. *Numer. Math.* **81**, 497–520.
- BARENBLATT, G. I. 1979 *Similarity, Self-Similarity, and Intermediate Asymptotics*. Consultants Bureau.
- BATCHELOR, G. K. 2000 *An Introduction to Fluid Dynamics*. Cambridge University Press.
- CANUTO, C., HUSSAINI, M. Y., QUARTERONI, A. & ZANG, T. A. 1988 *Spectral Methods in Fluid Dynamics*. Springer.
- CHAPMAN, R. F. 1998 *The Insects: Structure and Function*. Cambridge University Press.
- COOTER, R. J. & BAKER, P. S. 1977 Weis-Fogh clap and fling mechanism in *Locusta*. *Nature* **269**, 53–54.
- CROWDY, D. G. 2007 Schwarz–Christoffel mappings to unbounded multiply connected polygonal regions. *Math. Proc. Camb. Phil. Soc.* **142**, 319–339.
- CROWDY, D. 2009 The spreading phase in Lighthill’s model of the Weis-Fogh lift mechanism. *J. Fluid Mech.* **641**, 195–204.
- CROWDY, D. G. & MARSHALL, J. S. 2007 Computing the Schottky–Klein prime function on the Schottky double of planar domains. *Comput. Meth. Funct. Theor.* **7** (1), 293–308.
- CROWDY, D. G., SURANA, A. & YICK, K.-Y. 2007 The irrotational motion generated by two planar stirrers in inviscid fluid. *Phys. Fluids* **19**, 018103.
- EDWARDS, R. H. & CHENG, H. K. 1982 The separation vortex in the Weis-Fogh circulation-generation mechanism. *J. Fluid Mech.* **120**, 463–473.
- ELLINGTON, C. P. 1984 The aerodynamics of hovering insect flight. III. Kinematics. *Phil. Trans. R. Soc. Lond. B* **305**, 41–78.
- GRADSHTEYN, I. S. & RYZHIK, I. M. 1980 *Table of Integrals, Series, and Products*. Academic.
- HAUSSLING, H. J. 1979 Boundary-fitted coordinates for accurate numerical solution of multibody flow problems. *J. Comput. Phys.* **30**, 107–124.
- KOLOMENSKIY, D., MOFFATT, H. K., FARGE, M. & SCHNEIDER, K. 2010 Vorticity generation during the clap–fling–sweep of some hovering insects. *Theor. Comput. Fluid Dyn.* **24** (1–4), 209–215.
- KOLOMENSKIY, D. & SCHNEIDER, K. 2009 A Fourier spectral method for the Navier–Stokes equations with volume penalization for moving solid obstacles. *J. Comput. Phys.* **228**, 5687–5709.
- LEHMANN, F.-O., SANE, S. P. & DICKINSON, M. 2005 The aerodynamic effects of wing–wing interaction in flapping insect wings. *J. Exp. Biol.* **208**, 3075–3092.
- LIGHTHILL, M. J. 1973 On the Weis-Fogh mechanism of lift generation. *J. Fluid Mech.* **60** (1), 1–17.
- MAXWORTHY, T. 1979 Experiments on the Weis-Fogh mechanism of lift generation by insects in hovering flight. Part 1. Dynamics of the ‘fling’. *J. Fluid Mech.* **93** (1), 47–63.
- MAXWORTHY, T. 2007 The formation and maintenance of a leading-edge vortex during the forward motion of animal wing. *J. Fluid Mech.* **587**, 471–475.
- MICHELIN, S. & LLEWELLYN SMITH, S. G. 2009 An unsteady point vortex method for coupled fluid–solid problems. *Theor. Comput. Fluid Dyn.* **23**, 127–153.
- MILLER, L. A. & PESKIN, C. S. 2005 A computational fluid dynamics of ‘clap and fling’ in the smallest insects. *J. Exp. Biol.* **208**, 195–212.
- MILLER, L. A. & PESKIN, C. S. 2009 Flexible clap and fling in tiny insect flight. *J. Exp. Biol.* **212** (19), 3076–3090.
- MOFFATT, H. K. 1964 Viscous and resistive eddies near a sharp corner. *J. Fluid Mech.* **18** (1), 1–18.
- MOFFATT, H. K. & DUFFY, B. R. 1980 Local similarity solutions and their limitations. *J. Fluid Mech.* **96** (2), 299–313.
- SCHNEIDER, K. & FARGE, M. 2005 Numerical simulation of the transient flow behaviour in tube bundles using a volume penalization method. *J. Fluids Struct.* **20** (4), 555–566.
- SEDOV, L. I. 1965 *Two-Dimensional Problems in Hydrodynamics and Aerodynamics*. Interscience.
- SPEDDING, G. R. & MAXWORTHY, T. 1986 The generation of circulation and lift in a rigid two-dimensional fling. *J. Fluid Mech.* **165**, 247–272.
- SUN, M. & YU, X. 2003 Flows around two airfoils performing fling and subsequent translation and translation and subsequent clap. *Acta Mech. Sinica* **19**, 103–117.

- WAGNER, H. 1925 Über die Entstehung des dynamischen Auftriebes von Tragflügeln. *Z. Angew. Math. Mech.* **5**, 17–35.
- WEIS-FOGH, T. 1973 Quick estimates of flight fitness in hovering animals, including novel mechanisms for lift production. *J. Exp. Biol.* **59**, 169–230.
- WEIS-FOGH, T. 1975 Flapping flight and power in birds and insects, conventional and novel mechanisms. In *Swimming and Flying in Nature* (ed. T. Y. Wu, C. J. Brokaw & C. Brennen), vol. 2, pp. 729–762. Plenum.
- WU, J. C. & HU-CHEN, H. 1984 Unsteady aerodynamics of articulate lifting bodies. *AIAA Paper* 2184.